Supplemental Material for: Electronic layer decoupling driven by density-wave order in $La_4Ni_3O_{10}$

Ziqiang Guan,[1] Sophia F. R. TenHuisen,[1, 2] M. Tepie,[1] Yifeng Zhao,[3] Ezra Day-Roberts,[3] Harrison LaBollita,[3] Alexander M. Young,[1] Xiaomeng Cui,[1] Xinglong Chen,[4] Filippo Glerean,[1, 5] Carl Audric Guia,[1] Mark P. M. Dean,[5] Philip Kim,[1, 2] J. F. Mitchell,[4] Antia S. Botana,[3] Christopher C. Homes,[6] and Matteo Mitrano[1]

[1]*Department of Physics, Harvard University, Cambridge, Massachusetts 02138, USA*
[2]*John A. Paulson School of Engineering and Applied Sciences,*
Harvard University, Cambridge, Massachusetts 02138, USA
[3]*Department of Physics, Arizona State University, Tempe, Arizona 85287, USA*
[4]*Materials Science Division, Argonne National Laboratory, Lemont, Illinois 60439, USA*
[5]*Condensed Matter Physics and Materials Science Department,*
Brookhaven National Laboratory, Upton, New York 11973, USA
[6]*National Synchrotron Light Source II, Brookhaven National Laboratory, Upton, NY, USA*

(Dated: April 28, 2026)

S1. SAMPLE PREPARATION, OPTICAL EXPERIMENTAL METHODS, AND FULL TEMPERATURE-DEPENDENT DATASET

High-quality single crystals of $La_4Ni_3O_{10}$ were grown using a vertical optical-image floating zone furnace operating at high O_2 pressure according to the procedures described in Ref. [1]. The quality and orientation of the single crystals were confirmed by x-ray Laue diffraction. We note that, as in many oxygen-rich Ruddlesden-Popper nickelates, subtle deviations from ideal oxygen stoichiometry and/or occasional intergrowths cannot be excluded a priori, even when the average-structure diffraction is of high quality. However, in crystals grown nominally in the same way, the oxygen nonstoichiometry was found to be below the 1% level [1]. We note that our conclusions rely on robust optical observables and do not depend on resolving the fine details of the DW-modulated structure.

Two large single crystals (approximately $3 \times 2 \times 2$ mm^3) of $La_4Ni_3O_{10}$ were polished to expose an ab-plane and an ac^*-plane, respectively. The near-normal-incidence reflectivity $R(\omega)$ at ambient pressure was measured in the frequency range of 60-22,000 cm^{-1} using a Bruker Vertex 80v Fourier-transform infrared spectrometer (FTIR) and referenced with in situ gold evaporation [2].

We used unpolarized light to measure the ab-plane reflectivity on an ab-plane-polished sample. Polishing introduced a small misorientation of the crystal surface ($\sim 2°$), as verified by subsequent x-ray diffraction on the same sample. This misorientation slightly mixes c^*-axis signatures into the ab-plane FTIR measurement with unpolarized light, which in practice appears as a small reduction of the overall reflectivity and weak phonon-like peaks at the same frequencies as in the c^*-axis spectrum [3]. We correct for this mixing by subtracting the c^*-axis reflectivity contribution and renormalizing the result. This correction does not affect the conclusions of this article. Owing to the high ab-plane conductivity and reflectivity, we use a Hagen-Rubens extrapolation below the lowest measured frequency.

We used out-of-plane-polarized light to measure the c^*-axis reflectivity on an ac^*-plane-polished sample. For this configuration, we also performed polarization-resolved terahertz time-domain spectroscopy (THz-TDS) to extend the low-frequency data down to 30 cm^{-1}. We employed an echelon-based single-shot THz-TDS system [4, 5] pumped by 800 nm, 35 fs pulses from a 1 kHz Ti:sapphire amplifier. THz pulses were generated in a 0.5-mm-thick ⟨110⟩ ZnTe crystal and electro-optic sampling of the light reflected from the sample was carried out focusing on a 0.2-mm-thick ⟨110⟩ ZnTe sensor optically contacted to a 1-mm-thick ⟨100⟩ ZnTe substrate. The THz reflectivity was obtained by normalizing the THz spectrum of the sample to that of a gold reference measured under identical conditions. The entire THz-TDS apparatus operated under vacuum. The ac^* face was polished shortly prior to the optical experiment using a 0.1 μm final grit to ensure a fresh, high-quality surface. To determine the principal optical axes and suppress possible ab-plane leakage, we performed a polarizer-angle calibration on the ac^* face by measuring the ratio of FTIR interferogram amplitude from the sample to that from a reference mirror as a function of polarizer angle and fitting the result to a $\sin^2\theta$ dependence; the fitted minimum defines the extinction angle used for the c^*-axis measurement (uncertainty $< 1^\circ$), and residual leakage from a small angular error is proportional to $\sin^2(\Delta\theta)$, making the extracted c^* response insensitive to a few-degree mis-setting. Polarizers with high extinction ratios were used in all spectral ranges to minimize polarization leakage. Because the c^*-axis conductivity and reflectivity are lower and the low-frequency region contains many Lorentz modes, we fit the low-frequency reflectivity with a Drude model including a background dielectric permittivity (a simple ε_∞+Drude approximation) and use it to extrapolate below the lowest measured frequency [6].

The complex optical conductivity was determined via a Kramers-Kronig analysis of the measured reflectivity. For both the ab-plane and c^*-axis reflectivity, we use an x-ray atomic scattering factor for the high-frequency extrapolation [6]. We also tested different high-frequency extrapolation methods, such as assuming a constant reflectivity up to 10^6 cm^{-1} ($\sim$ 124 eV) followed by a free-electron (ω^{-4}) response. The complex optical conductivity calculated based on different methods shows no qualitative difference in the measured frequency range.

Fig. S1 shows the full temperature-dependent reflectivity and conductivity data set of both in-plane and out-of-plane polarization. The ab-plane response shows robust metallic behavior as the reflectivity approaches unity in the zero-frequency limit and keeps rising with decreasing temperature in the far-infrared range ($<$400 cm^{-1}). Suppression in the mid-infrared range (400-1000 cm^{-1}), together with the spectral weight transfer to higher frequency range, indicate the onset of a density wave energy gap below the transition temperature of 140 K. For the out-of-plane response, the low frequency ($<$ 100 cm^{-1}) reflectivity shows an upturn for temperatures above the DW transition, suggesting a finite Drude component. However, the Drude component is suppressed at low temperatures and remains relatively small compared to the Lorentzian phonon modes or the interband transitions as seen in the conductivity.

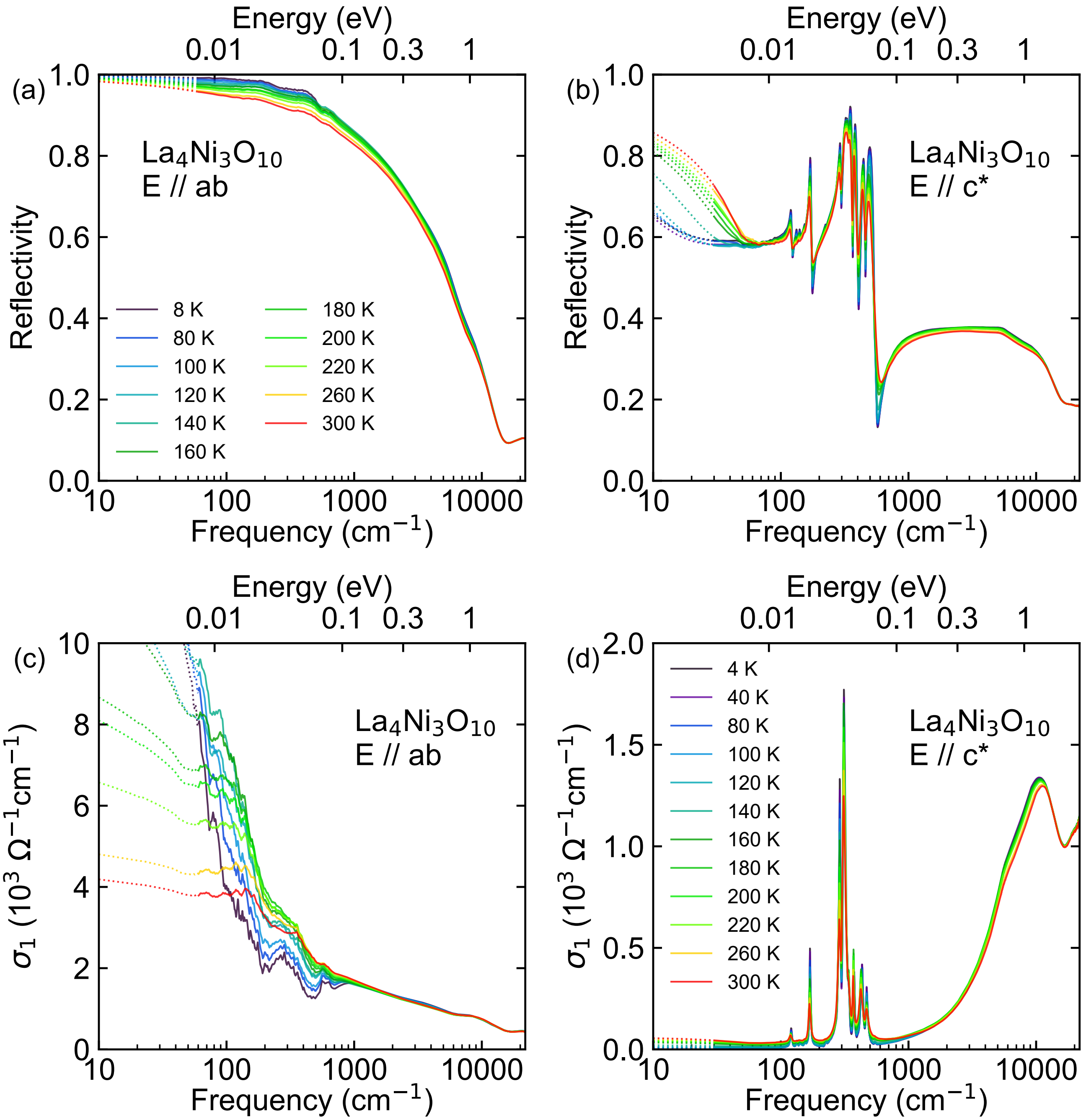

FIG. S1. Reflectivity (a)(b) and real part of optical conductivity (c)(d) over a broad frequency range at all measured temperatures. Out-of-plane ($E \parallel c^*$) and in-plane ($E \parallel ab$) are shown on the left and right, respectively. Dotted lines indicate the low-frequency extrapolations as described in experimental method Sec. S1.

S2. DFT ELECTRONIC STRUCTURE AND OPTICAL PROPERTIES

The electronic structure and optical properties calculations were performed using all-electron, full-potential DFT code WIEN2K [7]. We used the Perdew-Burke-Ernzerhof version of the generalized gradient approximation as the exchange-correlation functional [8]. All calculations were performed using the experimental structure with $P2_1/a$ symmetry at ambient pressure [1] in the nonmagnetic state. A 5×13×13 k-point grid was used for the Brillouin

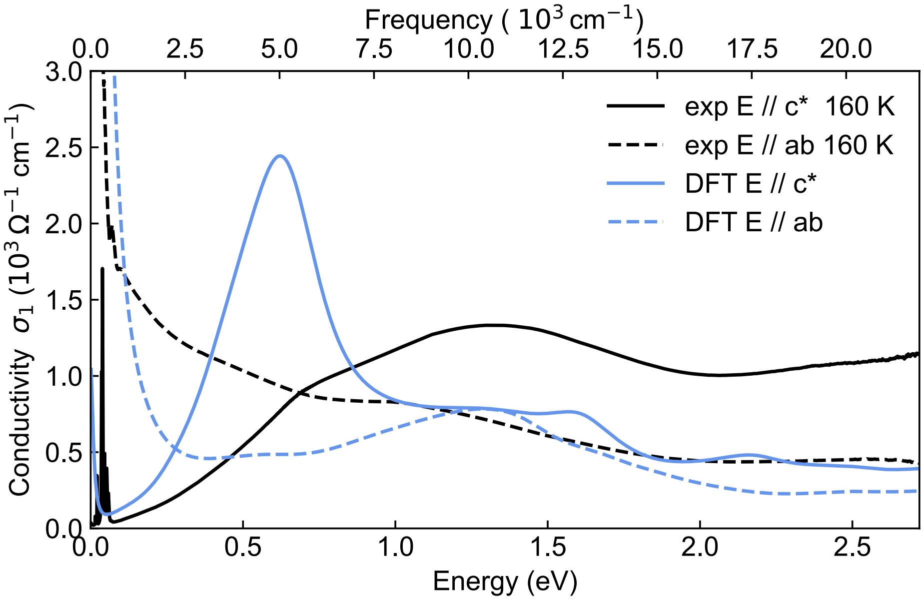

FIG. S2. Comparison of optical conductivity measured experimentally (exp) and calculated with DFT.

sampling in self-consistent calculations, while a denser k-point grid of 11×29×30 was used to accurately describe the optical properties. An $RK_{\max} = 7$ and muffin-tin radii of 2.38, 1.91, and 1.70 a.u. were used for La, Ni, O, respectively. The broadening factor (scattering rate) used to compute the interband contribution to the optical conductivity is set to be 0.1 eV. For the intraband contribution, the plasma frequency is directly obtained from DFT calculations, while the scattering rate (Drude width) is taken from fitted parameters in the experimental optical conductivity $\sigma(\omega)$ at 160 K. The in-plane optical conductivity is obtained by averaging the two inequivalent in-plane components.

Figure S2 presents the comparison between experimentally measured and DFT calculated real part of the optical conductivity. The DFT calculation shown here did not include a Hubbard U. Similarly to the experimental result, the DFT calculation also reveals a strong anisotropy reversal as a function of frequency. The DFT calculated out-of-plane optical conductivity exceeds the in-plane components substantially around 0.6 eV. However, the anisotropy crossover appears near 0.3 eV, much lower than the experimentally observed crossover energy. This discrepancy is to some extent expected as general DFT calculations usually underestimate the interband transition energies [9]. Electronic-correlation-induced mass-renormalization could also contribute to the underestimation of the interband transition energy, as suggested by previous ARPES results[10]. Further, the calculations were performed in the nonmagnetic state only and not in the DW state (where the Ni-O planes are decoupled via the nonmagnetic mirror layer).

Next, we analyze the orbital contribution to the anisotropic optical conductivity. Figure. S3 shows the DFT calculated band structure with Hubbard $U = 0$. Near the Fermi level, Ni $d_{x^2-y^2}$ and d_{z^2} bands dominate the optical transitions. By comparing the band structure with the optical conductivity, we identify that the main contributions to the in-plane interband conductivity arise from transitions between bands with dominant $d_{x^2-y^2}$ character, while the out-of-plane interband conductivity is mainly associated with transitions between bands of dominant d_{z^2} character. This orbital dependence of the optical conductivity can be understood from the spatial orientation of the two $3d$ orbitals of the Ni atom. The $d_{x^2-y^2}$ orbitals lie in the Ni-O plane and mainly contribute to electronic coupling within the plane, while the d_{z^2} orbitals extend along the c^*-axis and mainly contribute to the charge transport between layers. The difference in the orbital orientations naturally leads to the strong polarization dependence in the optical response.

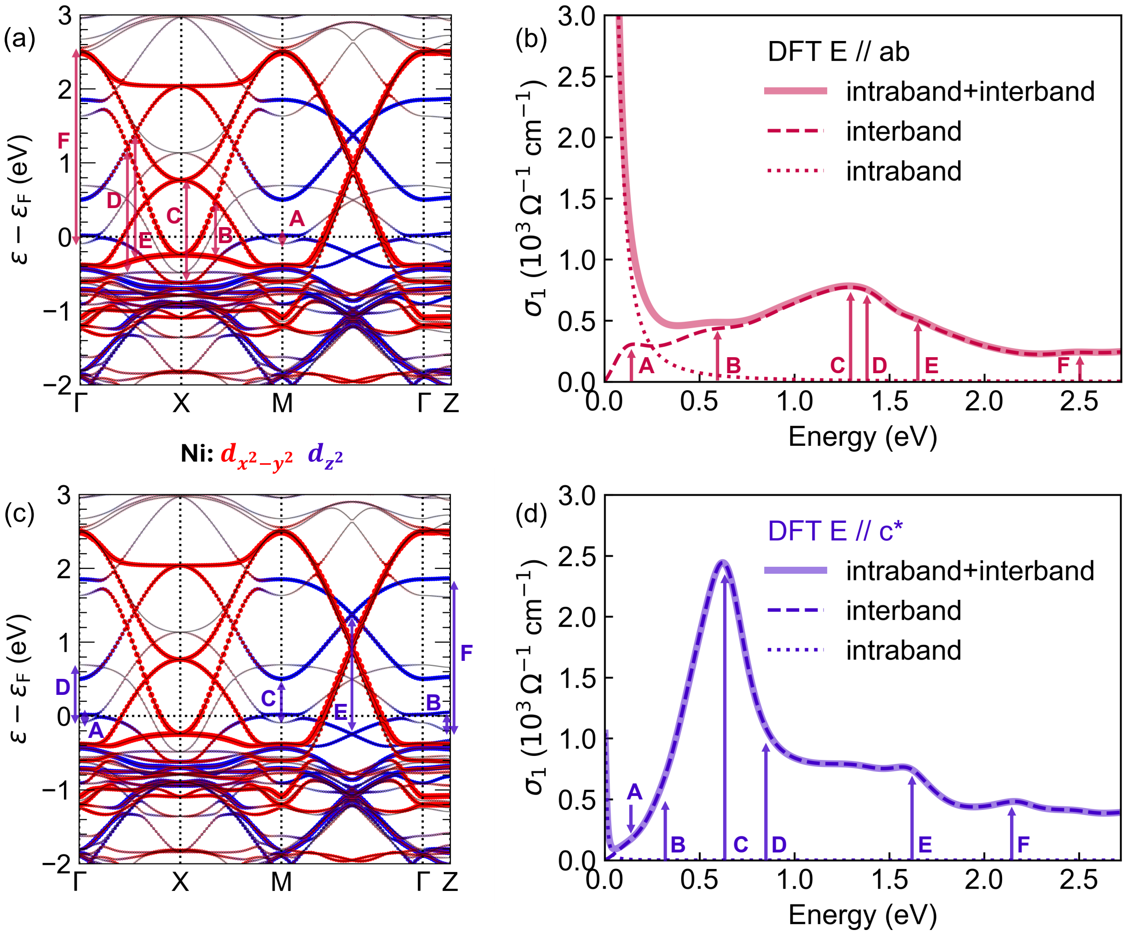

FIG. S3. DFT calculated band structure and optical conductivity of $La_4Ni_3O_{10}$. Panels (a) and (c) display identical band structures, colored to highlight the dominant orbital character: Ni $d_{x^2-y^2}$ components in red and d_{z^2} components in blue. These bands give rise to the distinct optical conductivities along the in-plane and out-of-plane directions, shown in (b) and (d), respectively. The total optical conductivity, along with its interband and intraband components, is presented for both polarizations. The arrows in (b) and (d) indicate the principal optical transitions, corresponding to the interband processes labeled in the band structures. The Fermi level is set to be 0 eV in panels (a) and (c).

S3. DENSITY WAVE ENERGY GAP EXTRACTION

The DW optical gap appears in the in-plane conductivity as a transfer of spectral weight from lower frequencies to higher frequencies. To visualize this redistribution without logarithmic compression, we also show $\sigma_{1,ab}(\omega)$ on a linear scale in Fig. S4, where the crossing near ~ 1000 cm^{-1} is readily visible. We extract the gap by analyzing the conductivity difference spectrum, $\Delta\sigma_1(\omega) = \sigma_1(\omega, T < T_{\mathrm{DW}}) - \sigma_1(\omega, T_{\mathrm{DW}})$. We take the spectrum just above the DW transition (140 K) as the normal-state reference to minimize unrelated temperature-dependent effects.

Fig. S5(a) compares the in-plane optical conductivities at 8 K and 140 K. The spectra show a suppression in the mid-infrared and an enhancement at higher frequencies, crossing near 1000 cm^{-1}. We attribute this spectral-weight transfer to the opening of the DW gap, since a simple narrowing of the Drude peak cannot account for the high-frequency enhancement. Fig. S5(b) shows the 8 K difference conductivity $\Delta\sigma_1(\omega)$; the zero-crossing point (black arrow) defines the optical gap, $2\Delta = 112$ meV. The resulting DW gap, $\Delta = 56$ meV, agrees with a previous FTIR report on the same material (61 meV) [11]. For $T_{\mathrm{DW}} = 140$ K, this yields $2\Delta/k_B T_{\mathrm{DW}} \approx 9.3$, far above the weak-coupling value of 3.52, highlighting the unconventional nature of the DW transition in $La_4Ni_3O_{10}$.

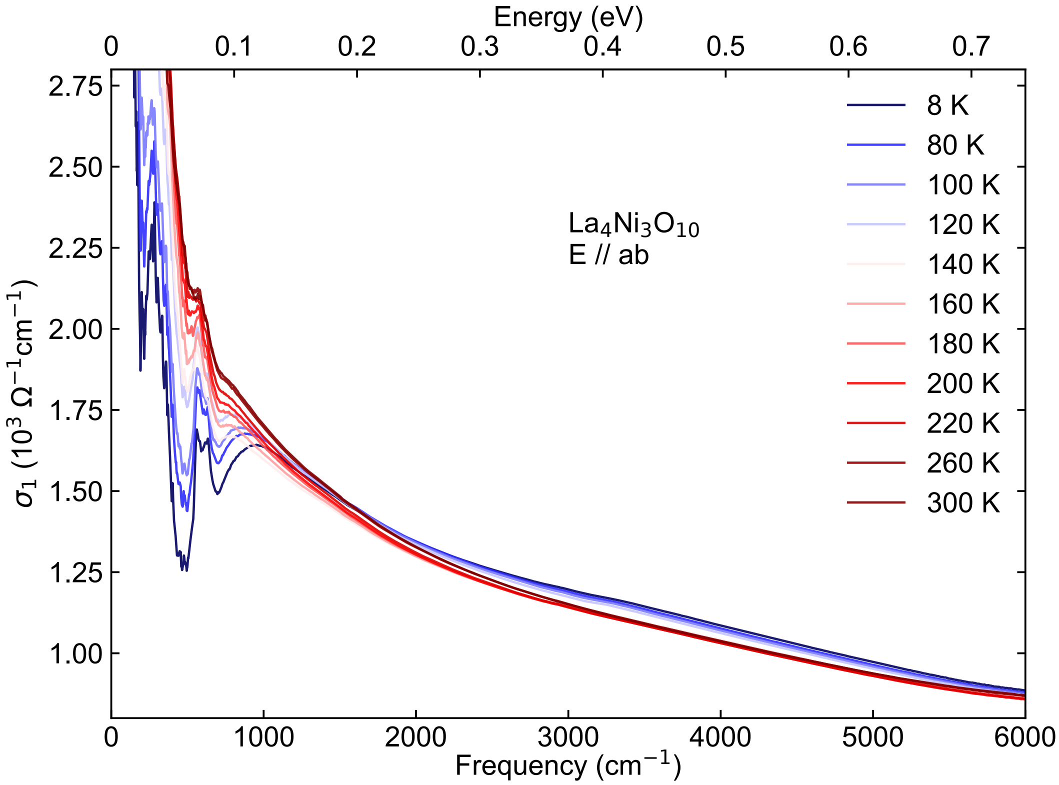

FIG. S4. Linear-scale view of the in-plane real optical conductivity $\sigma_{1,ab}(\omega)$ of La$_4$Ni$_3$O$_{10}$ over 0-6000 cm^{-1}, with low-T spectra shown in cooler (blue-like) colors and high-T spectra shown in warmer (red-like) colors. A clear DW-induced spectral-weight transfer is visible: below $\sim$ 1000 cm^{-1} the high-T curves lie above the low-T curves, while above $\sim$ 1000 cm^{-1} the trend reverses (low-T curves exceed high-T curves), producing an approximate crossing near 1000 cm^{-1}.

The temperature dependence of energy gap Δ [Fig. S5(c)] follows a mean-field behavior. We obtain the mean-field curve by solving the self-consistent BCS gap equation and normalizing by the maximum gap and the DW transition temperature. To estimate uncertainties, we conservatively assume a relative reflectivity error of $\pm 0.5\%$ between temperatures, rescale $R(\omega)$ at all temperatures by factors of 1.005 and 0.995, recompute the corresponding conductivities, and re-extract Δ; we take the difference between the gap values from the scaled reflectivities as the error bar, providing a conservative estimate of uncertainty from reflectivity errors. While the number of data points near T_{DW} is limited, the observed $\Delta(T)$ suggests that the DW transition is close to continuous and likely driven by an SDW instability, consistent with the Landau analysis of Ref. [12].

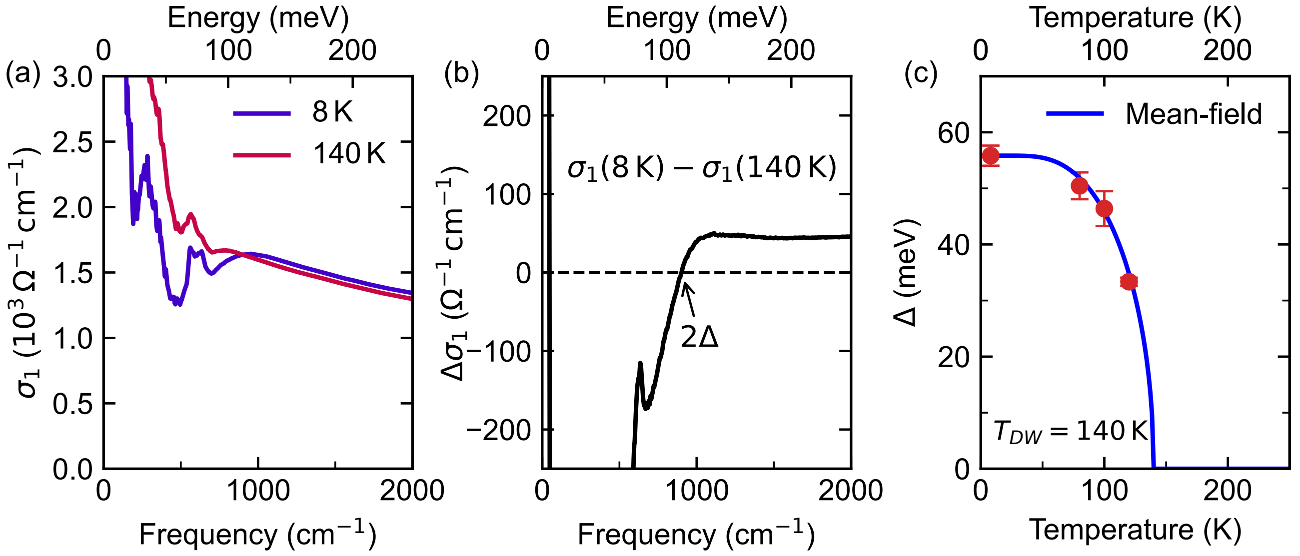

FIG. S5. Density wave energy gap and mean-field behavior. (a) and (b) display the in-plane optical conductivities and their difference at the lowest measured temperature 8 K, and just above the DW transition at 140 K. The opening of the DW energy gap 2Δ is illustrated by the spectral weight transfer and crossing close to $1000\,\mathrm{cm}^{-1}$. The evolution of energy gap Δ with temperature is shown in panel (c). The solid blue line denotes the mean-field behavior.

S4. ELECTRONIC CORRELATION CALCULATION

We quantify electronic correlations in $La_4Ni_3O_{10}$ using the ratio of experimental to band-theory kinetic energy, $K_{\mathrm{exp}}/K_{\mathrm{DFT}}$ [13–15]. To avoid contributions from interband transitions and phonons, we relate the kinetic energy to the Drude plasma frequency and compute $K_{\mathrm{exp}}/K_{\mathrm{DFT}} = \omega^2_{p,exp}/\omega^2_{p,cal}$. Because standard DFT does not capture DW effects, we use the experimental optical conductivity at 160 K (just above the DW transition) as the reference experimental spectrum. We perform the DFT calculation without including a Hubbard U. For the in-plane direction, a Drude+ε_∞ fit to the measured $\sigma_{1,ab}(\omega)$ yields $\omega^{ab}_{p,\mathrm{exp}} = 9855\ \mathrm{cm}^{-1}$ (1.222 eV), while DFT gives $\omega^{ab}_{p,\mathrm{cal}} = 2.511$ eV, resulting in $K^{ab}_{\mathrm{exp}}/K^{ab}_{\mathrm{DFT}} = 0.237$, consistent with previous reports [11, 15]. For the out-of-plane direction, we obtain $\omega^{c^*}_{p,\mathrm{exp}} = 402\ \mathrm{cm}^{-1}$ (0.050 eV) and $\omega^{c^*}_{p,\mathrm{cal}} = 0.278$ eV, giving $K^{c^*}_{\mathrm{exp}}/K^{c^*}_{\mathrm{DFT}} = 0.032$.

Based on kinetic-energy ratios extracted from the optical plasma frequencies, $La_4Ni_3O_{10}$ is a moderately correlated metal in the in-plane direction, with $K^{ab}_{\mathrm{exp}}/K^{ab}_{\mathrm{DFT}} = 0.237$, while the out-of-plane response is strongly suppressed, yielding $K^{c^*}_{\mathrm{exp}}/K^{c^*}_{\mathrm{DFT}} = 0.032$. As summarized in Fig. S6, these values place $La_4Ni_3O_{10}$ in an intermediate regime relative to other layered nickelates and correlated oxides. The in-plane response is comparable to $BaFe_2As_2$, where multiorbital physics is important, whereas the out-of-plane response resembles $La_3Ni_2O_7$ and La_2CuO_4, which lie close to the Mott-insulating limit. This pronounced anisotropy reflects the layered crystal structure and the strongly reduced interlayer charge dynamics.

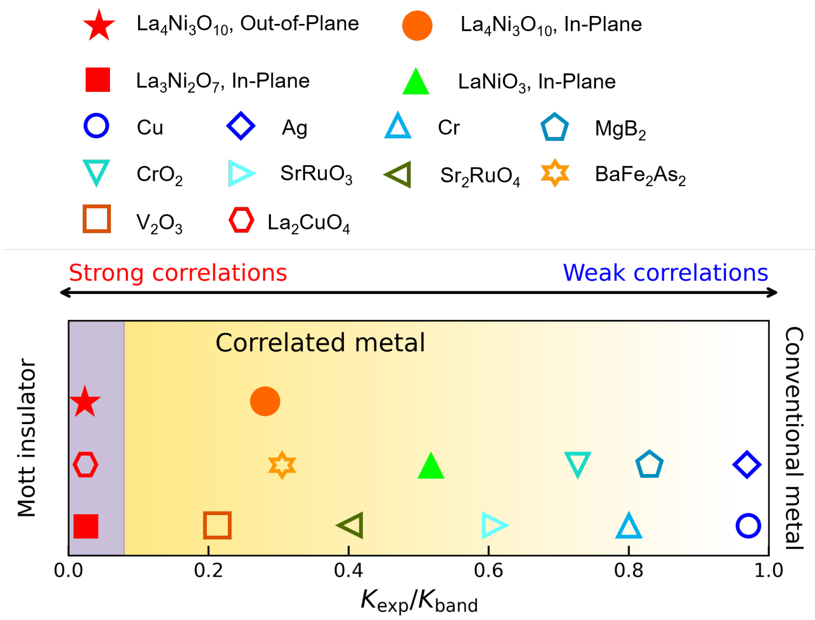

FIG. S6. Kinetic-energy ratio $K_{\text{exp}}/K_{\text{band}}$ for $La_4Ni_3O_{10}$ along the in-plane and out-of-plane directions, compared with the related nickelates $La_3Ni_2O_7$ and $LaNiO_3$, and with other representative materials. For clarity, nickelates are shown as solid symbols and other materials as open symbols. $La_4Ni_3O_{10}$ is highlighted by a solid red star (out of plane) and a solid orange circle (in plane). Values of $K_{\text{exp}}/K_{\text{band}}$ are taken from Refs. [13, 15, 16] and references therein.

S5. DRUDE-LORENTZ FITTING

We use the multi-component Drude-Lorentz model to quantitatively analyze the temperature dependence of free carrier density, scattering rate, and phonon modes. The optical response of the material is modeled using a standard Drude-Lorentz formalism for the dimensionless complex dielectric function [6, 17],

$$\varepsilon(\omega) = \varepsilon_\infty - \sum_j \frac{\omega_{p,j}^2}{\omega^2 + i\gamma_j\omega} + \sum_k \frac{\omega_{p,k}^2}{\omega_{0,k}^2 - \omega^2 - i\gamma_k\omega}, \tag{S1}$$

where the first summation describes the free-carrier response using one or more Drude terms, characterized by Drude plasma frequencies $\omega_{p,j}$ and Drude scattering rates γ_j. The second summation represents bound excitations modeled as Lorentz oscillators with resonance frequencies $\omega_{0,k}$, oscillator strengths $\omega_{p,k}$, and damping constants γ_k, which captures infrared-active phonons, interband transitions, and other finite energy excitations. The term ϵ_∞ is the high-frequency dielectric constant accounting for polarization processes that occur at energies well above the spectral window explicitly modeled by the Drude and Lorentz terms. Physically, ϵ_∞ incorporates mostly the cumulative contribution of core-electron and high-energy valence-electron screening that respond essentially instantaneously on the timescale of infrared excitations. As such, ϵ_∞ provides a constant background that ensures the correct high-frequency limit of the dielectric function and should not be interpreted as the static dielectric constant.

The complex optical conductivity $\sigma(\omega)$ is directly related to the dielectric function via

$$\sigma(\omega) = \frac{\omega\,[\varepsilon(\omega) - 1]}{59.958\,i}, \tag{S2}$$

where the frequency ω is expressed in units of cm^{-1} and the resulting conductivity is obtained in units of $\Omega^{-1}\text{cm}^{-1}$. The numerical factor $59.958 \approx 60$ arises from unit conversion and corresponds to $Z_0/2\pi$, where Z_0 is the vacuum impedance [6, 17]. We use this formula to simultaneously fit the real and imaginary parts of the complex optical conductivity.

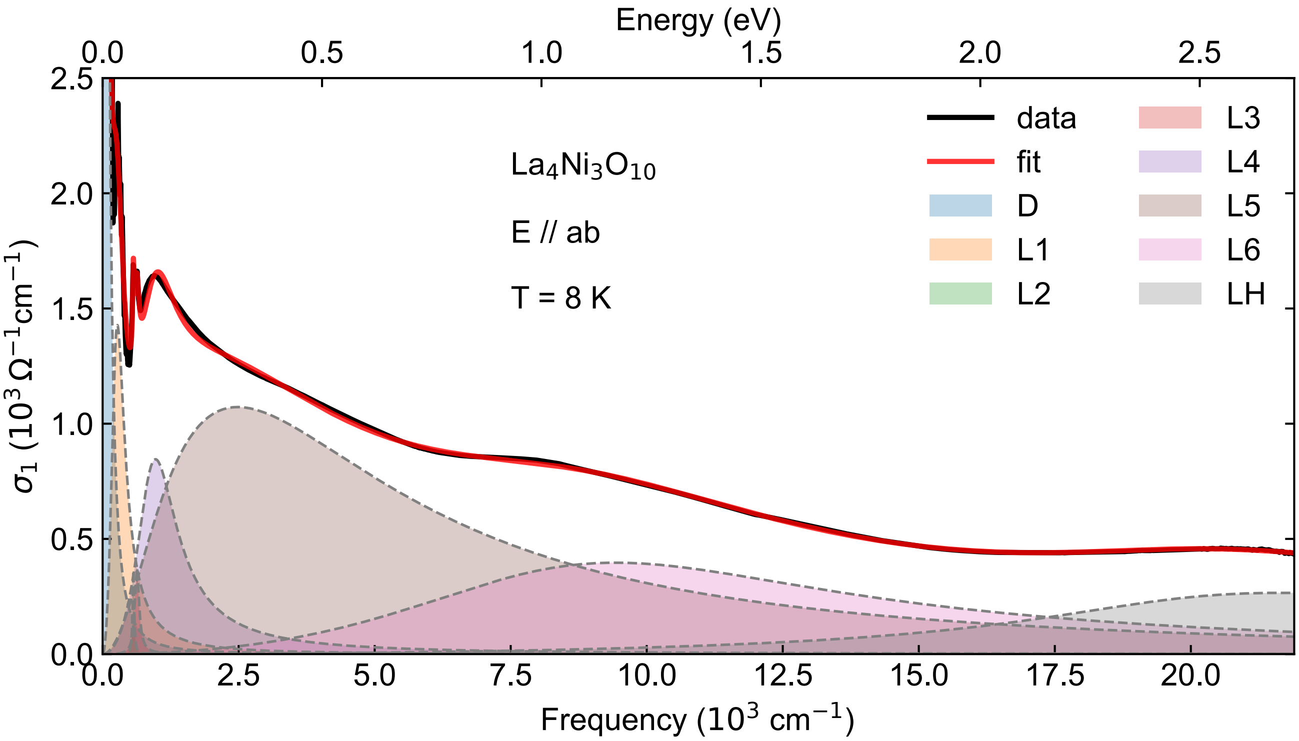

FIG. S7. The in-plane experimental $\sigma_1(\omega)$ (black curve) at 8 K and the Drude-Lorentz fitting result (red curve). Individual Drude and Lorentz components are shown as shaded areas.

We performed Drude-Lorentz fits at all temperatures for both the in-plane and out-of-plane optical conductivity; as an example, Fig. S7 shows the Drude-Lorentz fit to the in-plane optical conductivity at 8 K. We model multiple interband transitions with a set of Lorentz oscillators and include a phonon-like feature near 600 cm^{-1}. The fitted interband structure broadly follows DFT, although the oscillator strengths differ quantitatively, and fewer distinct modes are resolved experimentally, consistent with substantial spectral broadening.

In RP nickelates, the low-frequency response is sometimes parameterized with multiple Drude components to reflect multiband character and possible orbital-dependent scattering [11, 16]. When these intraband contributions are not spectroscopically resolved, however, such decompositions are not unique and increase correlations among parameters. Here, the low-frequency conductivity is a single, smooth Drude-like component, without clear signatures that uniquely require multiple Drude terms. Hence, we adopt a minimal intraband description to capture the essential charge dynamics while limiting model dependence.

To make the temperature evolution of the in-plane Drude-Lorentz analysis more transparent, we also compare representative fits above and below the DW transition in Fig. S8, showing the decomposition of $\sigma_{1,ab}(\omega)$ at 8 K and 160 K. We focus on the low-frequency range $\omega < 5000$ cm^{-1}, where the DW-related changes are most evident, while the higher-energy interband structure remains largely unchanged. In both cases, the conductivity is captured by a single Drude term together with a set of Lorentz oscillators that represent the low-energy phonon-like features and higher-energy interband transitions. Upon cooling into the DW state, the Drude response becomes weaker and sharper, with spectral weight transferred to finite frequency. The corresponding fit parameters of $\sigma_{1,ab}(\omega)$ in the low-frequency range are summarized in Table S1. In particular, the phonon-like structure near 600 cm^{-1} appears as a single broadened Lorentz component at 160 K, but resolves into two distinct components at 8 K as the low-temperature response sharpens.

To obtain a robust estimate of the in-plane dc resistivity from optics, we also analyze the low-frequency response using a simplified Drude+ε_∞ model. This approach is applied only within a restricted low-energy window that lies

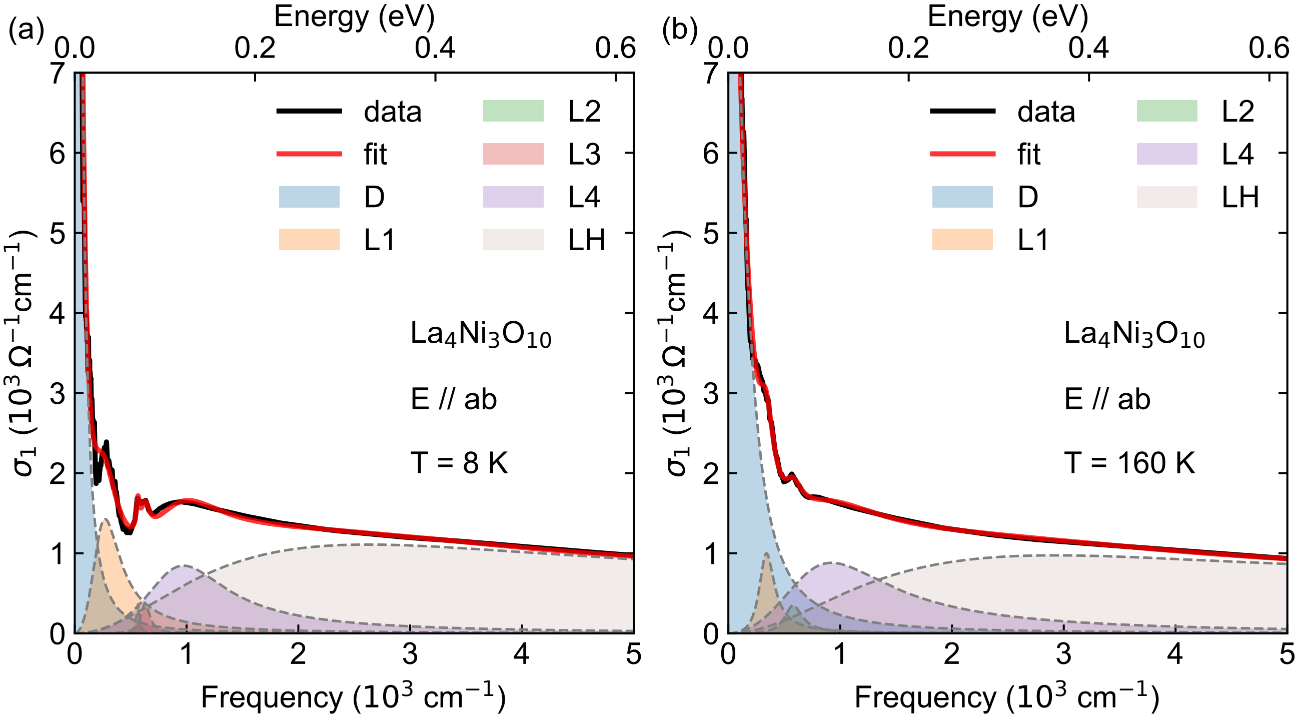

FIG. S8. Comparison of the in-plane experimental $\sigma_1(\omega)$ (black curves) and Drude-Lorentz fitting results (red curves) for $\mathrm{La_4Ni_3O_{10}}$ at 8 K and 160 K. Individual Drude and Lorentz components are shown as shaded areas. For visual clarity, the higher-frequency Lorentz components are combined into a single shaded contribution labeled LH. At 8 K, the low-frequency phonon-like structure near 600 $\mathrm{cm^{-1}}$ is resolved into two components (L2 and L3), whereas at 160 K these features are broadened and described by a single effective Lorentz oscillator (L2).

below the dominant phonon features and well below the onset of interband transitions, so that the free-carrier response is captured without relying on detailed modeling of higher-frequency Lorentz oscillators. In this low-frequency analysis, the contributions from phonons and interband transitions are effectively absorbed into a background dielectric constant ε_∞. The dielectric function is parametrized as

$$\varepsilon(\omega) = \varepsilon_\infty - \frac{\omega_p^2}{\omega^2 + i\gamma\omega}, \qquad \sigma(\omega) = \sigma_1(\omega) + i\sigma_2(\omega) = \frac{\omega\,[\varepsilon(\omega) - 1]}{59.958\,i}, \tag{S3}$$

and the dc conductivity is obtained from the $\omega \to 0$ limit of the fitted Drude term, $\sigma_{\mathrm{dc}} \propto \omega_p^2/\gamma$ (with the resistivity inferred from optics $\rho^{\mathrm{opt}} = 1/\sigma_{\mathrm{dc}}$ in the corresponding units). This simplified procedure reduces sensitivity to the detailed phonon/interband modeling at higher energies while still capturing the intrinsic temperature dependence of the low-energy carrier dynamics.

To better illustrate the temperature evolution of the low-frequency extrapolation, we include an expanded version of Fig. 2a-d for a denser temperature sampling, showing both the measured low-frequency optical conductivity and the corresponding Drude+ε_∞ fits.

We also compare two fitting strategies for the in-plane response in Fig. S10: (i) a full-range Drude-Lorentz fit over the entire measured window and (ii) a simple single Drude+ε_∞ fit. The extracted plasma frequency, scattering rate, and DC resistivity from the two approaches agree within uncertainties, supporting the Drude+ε_∞ analysis used in the main text as a reliable description of the in-plane free-carrier response.

For the out-of-plane response, the Drude spectral weight is much smaller, so full-range Drude-Lorentz fits become dominated by higher-frequency contributions. The resulting low-energy Drude parameters depend sensitively on the high-frequency modeling and are therefore not robust. We thus avoid full-range Drude-Lorentz fits for the c-axis data and instead rely on a low-frequency Drude+ε_∞ analysis.

TABLE S1. Drude-Lorentz fit parameters for the in-plane (E ∥ ab) optical conductivity $\sigma_1(\omega)$ of $La_4Ni_3O_{10}$ at 8 K and 160 K, in the low-frequency range ($\omega < 5000$ cm^{-1}). ω_0, ω_p, and γ denote resonance frequencies, plasma frequencies (oscillator strengths), and scattering rates (damping constants), respectively. At 8 K, two phonon-like components near 600 cm^{-1} are individually resolved (L2 and L3); at 160 K, thermal broadening of the Drude and phonon-like components prevents L2 and L3 from being individually resolved and they are instead described by a single Lorentz component (L2) in the fit.

	8 K			160 K		
Component	ω_0 (cm^{-1})	ω_p (cm^{-1})	γ (cm^{-1})	ω_0 (cm^{-1})	ω_p (cm^{-1})	γ (cm^{-1})
D	—	8588 ± 2	38.1 ± 0.1	—	9661 ± 4	150.9 ± 0.2
L1	$271 \pm {<1}$	5125 ± 19	307 ± 2	$341 \pm {<1}$	3138 ± 42	164 ± 2
L2	565 ± 1	848 ± 45	33 ± 3	580 ± 2	2000 ± 147	191 ± 15
L3[a]	629 ± 2	1466 ± 71	96 ± 8	—	—	—
L4	973 ± 4	6805 ± 208	913 ± 27	923 ± 9	8072 ± 405	1233 ± 59
L5	2483 ± 46	19572 ± 69	5958 ± 22	2713 ± 88	18972 ± 153	6436 ± 57

[a] At 160 K, L2 and L3 are not individually resolved due to thermal broadening; they are fitted as a single component (L2).

We observe that, in the in-plane response, the squared Drude plasma frequency ω_p^2, which is proportional to the effective free-carrier density, is reduced by approximately 25% upon cooling from high temperature to low temperature. This suppression indicates a partial depletion of the in-plane Fermi surface, consistent with the opening of a density-wave-induced gap that removes a fraction of the itinerant carriers [11].

Fig. S11 shows the Drude-Lorentz fit to the out-of-plane optical conductivity at 4 K as an example. We model high-energy interband transitions (> 1000 cm^{-1}) with a set of Lorentz oscillators, while we defer the detailed Drude-Lorentz analysis of phonons below 600 cm^{-1} to Sec. S7. As for the in-plane response, the fitted interband structure broadly agrees with DFT, although the oscillator strengths differ quantitatively and fewer modes are resolved experimentally, consistent with substantial spectral broadening.

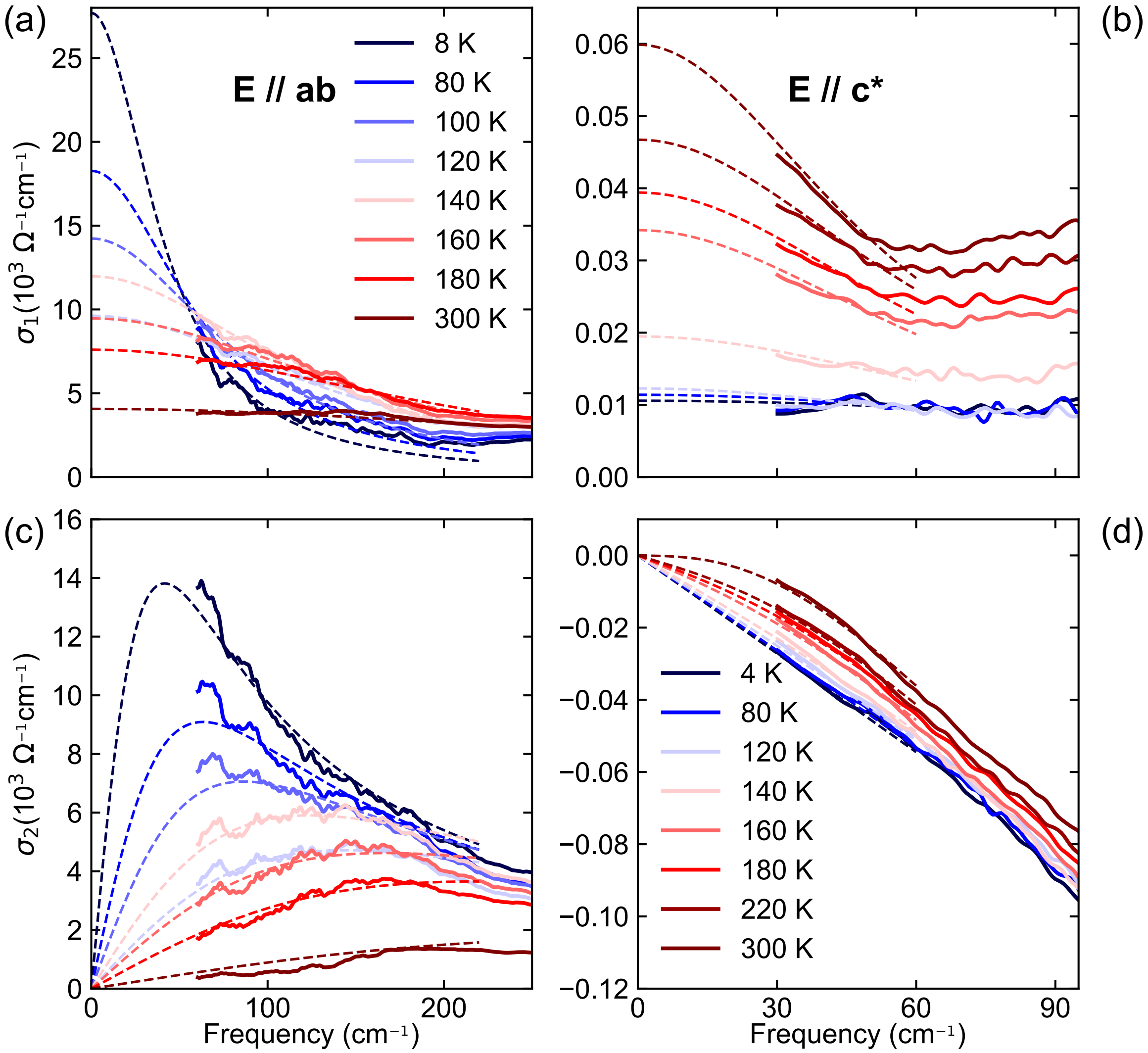

FIG. S9. Expanded version of Fig. 2a-d showing the low-frequency optical conductivity spectra (and the corresponding low-frequency Drude+ε_∞ fits) for a denser set of temperatures to better illustrate the temperature evolution and the dc extrapolation procedure.

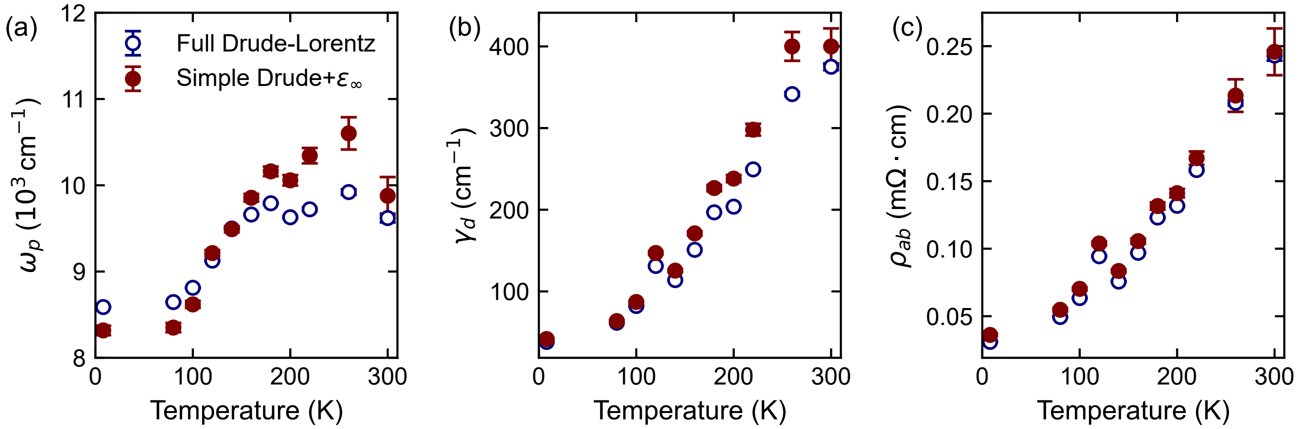

FIG. S10. Comparison of (a) in-plane Drude plasma frequency ω_p, (b) scattering rate γ_d, and (c) DC resistivity ρ_{ab} obtained from full-range Drude-Lorentz fitting (blue open circles) and low-frequency Drude+ε_∞ analysis (red filled circles) and as functions of temperature.

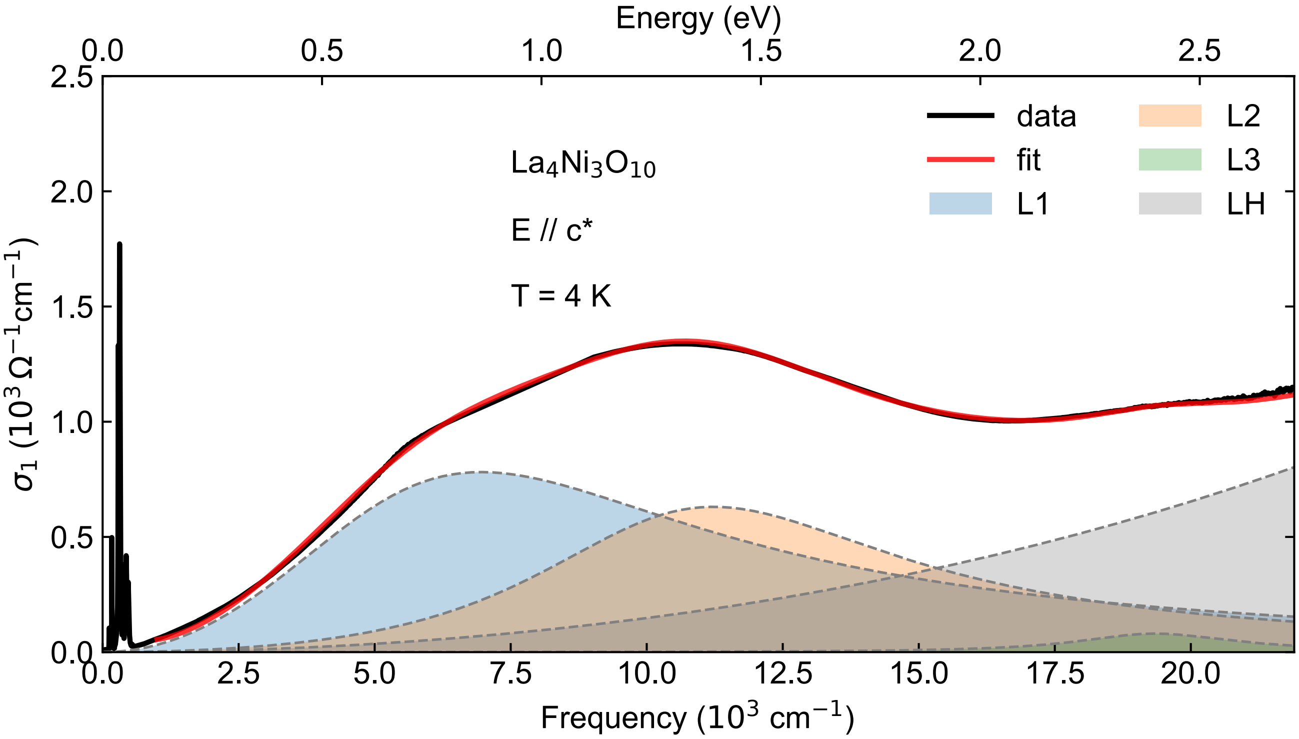

FIG. S11. Out-of-plane experimental $\sigma_1(\omega)$ (black curve) at 4 K and the Drude-Lorentz fit (red curve). Individual Lorentz components are shown as shaded areas.

S6. TRANSPORT RESISTIVITY

To further validate the temperature-dependent anisotropy extracted from the optical conductivity, we compare the DC resistivity inferred from optics with transport measurements. Transport resistivity carries inherent systematic uncertainties, most notably geometric factors used to convert resistance to resistivity, and overall uncertainties can approach an order of magnitude. A major advantage of optical spectroscopy is that it provides low-frequency limit resistivity free from the geometric uncertainties. For this reason, in comparing to transport we apply an overall rescaling factor to the transport data to account for its absolute uncertainty.

For the in-plane resistivity, we use published transport data from Ref. [1], shown as the cardinal red dashed line in Fig. S12 after applying a uniform rescaling factor of 0.15. Since no out-of-plane resistivity has been reported for $La_4Ni_3O_{10}$, we measured ρ_{c^*} using a standard four-probe technique on a polished ac^*-plane sample, varying temperature from 10 K to 300 K in a He^4 gas-flow cryostat. The measured out-of-plane $\rho_{c^*}(T)$ is also rescaled by a constant factor for plotting in Fig. S12, to align with the optically extrapolated DC resistivity. We note that in highly anisotropic systems such as $La_4Ni_3O_{10}$ it is difficult to eliminate mixing of in- and out-of-plane channels in a conventional four-probe geometry, and some sample-to-sample dispersion is also expected [1, 18, 19]. With these caveats in mind, the temperature dependence of our measured $\rho_{c^*}(T)$ closely resembles the reported out-of-plane resistivity trend of $Pr_4Ni_3O_{10}$ in Ref. [20]. Overall, the in-plane and out-of-plane resistivities inferred from the optical Drude analysis are in reasonable agreement with the transport data at the level of temperature trends. We emphasize that, due to uncertainties associated with the experimental configuration and sample-to-sample dispersion, the absolute value of ρ_{c^*}/ρ_{ab} should be taken as an estimate, while the temperature trend is the more robust result.

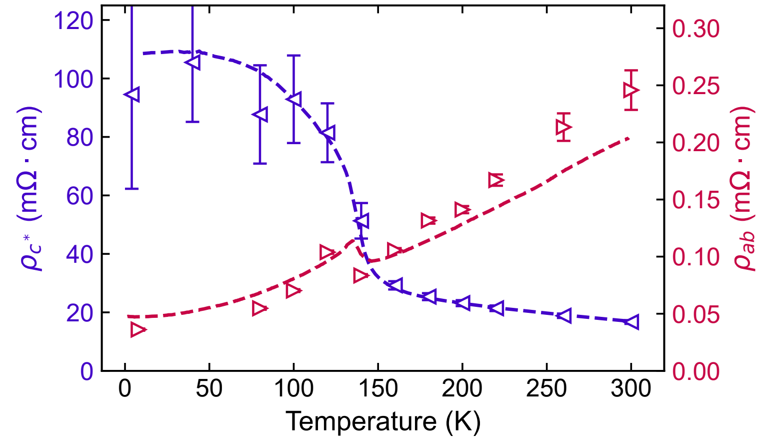

FIG. S12. Comparison between DC resistivity extracted from optical (triangles with error bars) and transport measurements (broken lines) on $La_4Ni_3O_{10}$ along both in-plane and out-of-plane directions. The in-plane transport resistivity ρ_{ab} data are adapted and rescaled from Ref. [1].

S7. PHONON MODES: FITTING

We fit the c^*-axis optical conductivity with a Drude-Lorentz model over the full temperature range, restricting the window to $\omega < 600$ cm^{-1} to include all observed infrared-active phonons while excluding higher-energy interband transitions. Fits at 4 K (Fig. S13) and 160 K (Fig. S14) are shown as representative examples well below and above the DW transition, respectively. In both cases, simultaneous fits to the real and imaginary parts of the complex conductivity capture the main features, enabling a systematic analysis of the phonon evolution with temperature.

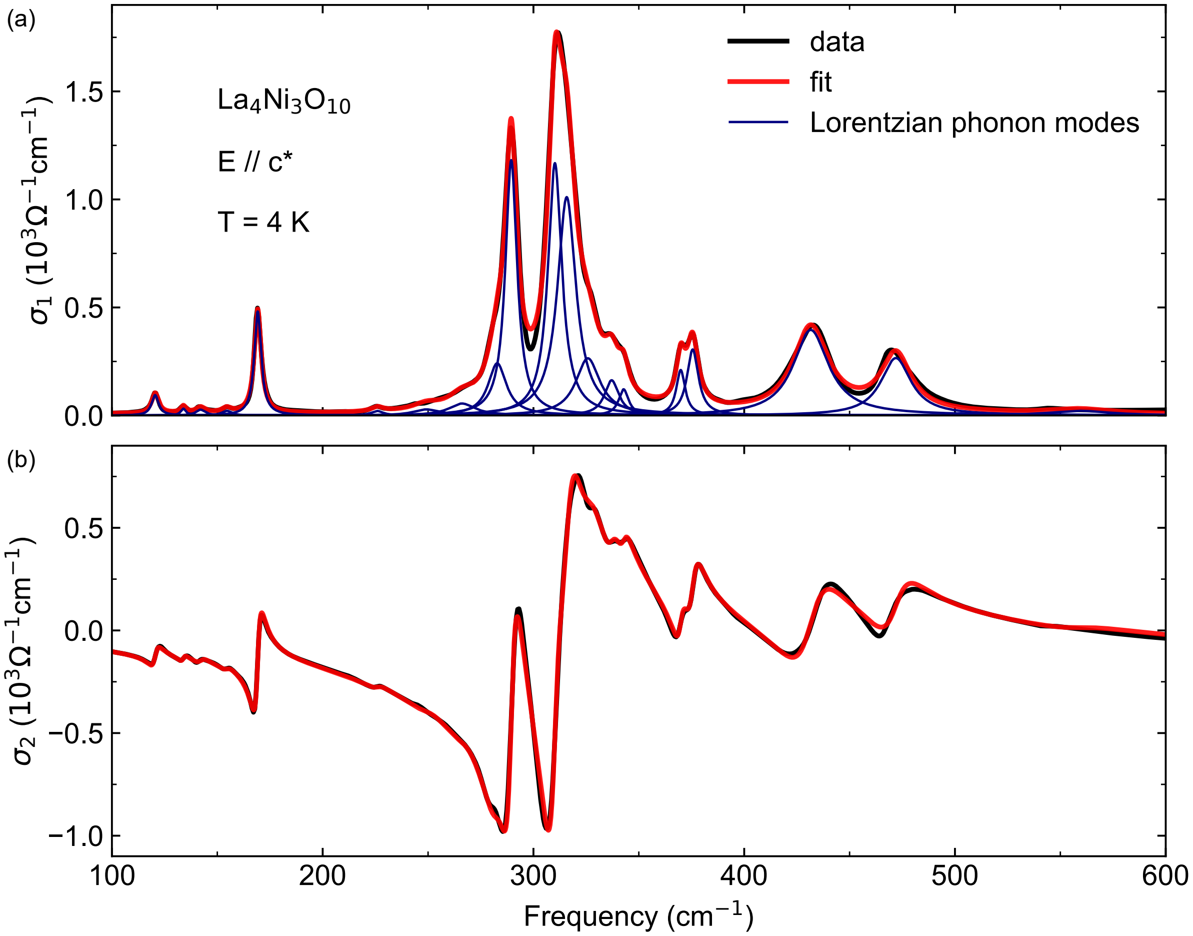

FIG. S13. Real and imaginary optical conductivity $\sigma_1(\omega)$ and $\sigma_2(\omega)$ at 4 K in the range of 100-600 cm^{-1}. The solid red line is the Drude-Lorentz fit of the experimental data (black solid line). Thin navy solid lines correspond to individual Lorentzian phonon modes. We identify a total of 20 modes at 4 K.

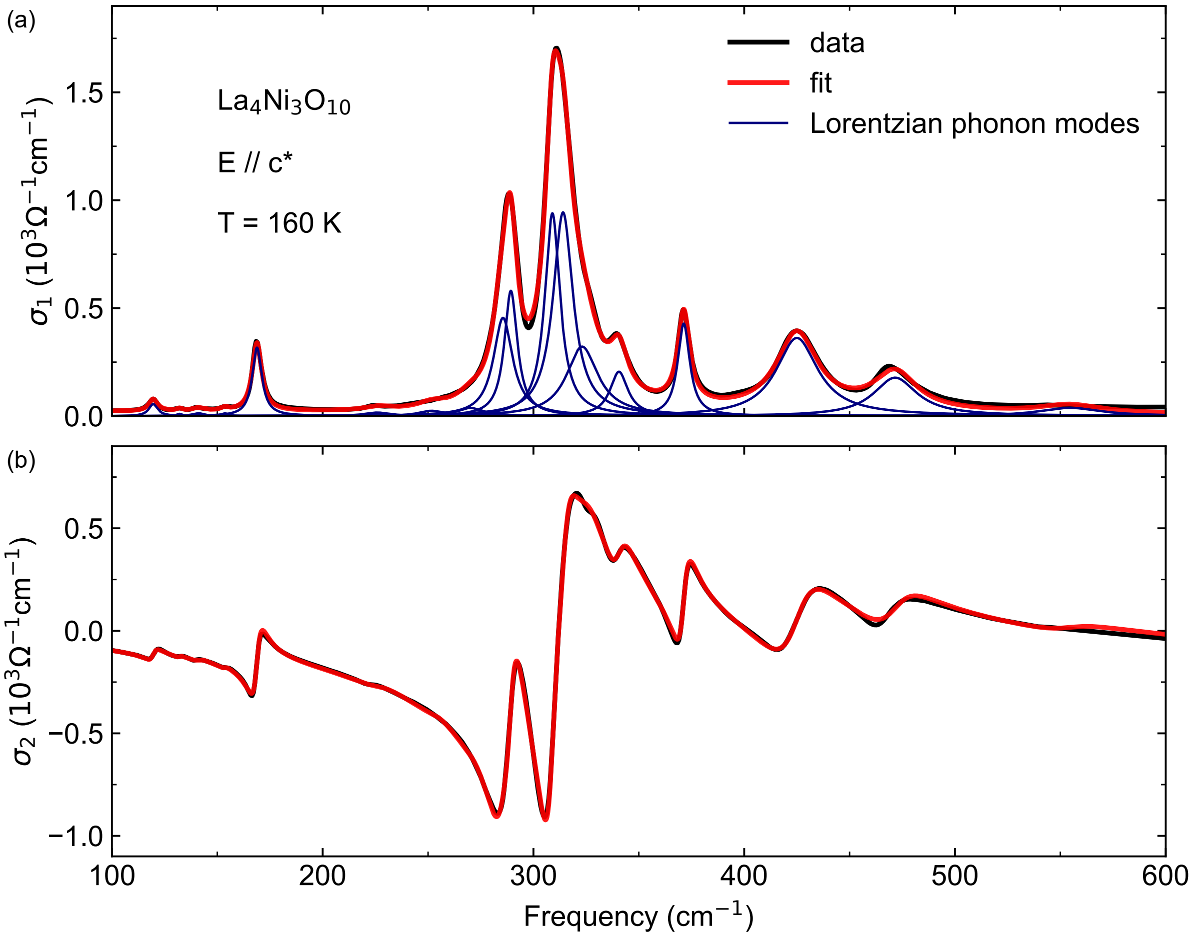

FIG. S14. Real and imaginary optical conductivity $\sigma_1(\omega)$ and $\sigma_2(\omega)$ at 160 K in the range of 100-600 cm^{-1}. The solid red line is the Drude-Lorentz fit of the experimental data (black solid line). Thin navy solid lines correspond to individual Lorentzian phonon modes. We identify a total of 18 modes at 160 K.

S8. PHONON MODES: COMPARISON WITH DFT

At ambient pressure, $La_4Ni_3O_{10}$ crystallizes in the monoclinic $P2_1/a$ structure and the average structure (fundamental Bragg peaks) shows no resolved average space-group change across the DW transition[18, 19, 21]. This structure with two formula units per primitive unit cell ($Z = 2$) supports a total of 102 normal modes at the Brillouin zone center: 3 acoustic and 99 optical modes. These modes decompose into $24A_g + 26A_u + 24B_g + 25B_u$ representations, where the odd-parity A_u and B_u modes are infrared-active and the even-parity A_g and B_g modes are Raman-active. In the conventional monoclinic $P2_1/a$ setting (unique b axis), the infrared-active modes decompose into A_u modes with dipole moments primarily along b, and B_u modes with dipole moments in the ac plane. Thus, an out-of-plane polarized experiment is expected to predominantly probe B_u modes. The monoclinic tilt angle ($\beta \approx 100.8^\circ$, i.e. $\sim 11^\circ$ between the crystallographic c direction and the experimental out-of-plane c^* direction [1]) together with crystal twinning effects and a small (possible) miscut can mix components, so both A_u and B_u modes may acquire finite intensity for the out-of-plane measurement.

Given the large number of symmetry-allowed optical modes and the monoclinic symmetry, we use first-principles calculations to guide the identification of corresponding modes. We perform phonon calculations within density functional theory using the finite-displacement method. We carry out the electronic-structure calculations with the Vienna *ab initio* Simulation Package (VASP) using the GGA-PBE exchange-correlation functional [8]. We base the calculations on the experimentally determined monoclinic $P2_1/a$ structure of $La_4Ni_3O_{10}$, with structural data taken from Ref. [1]. We obtain interatomic force constants with PHONOPY[22] by finite displacements in a $2\times2\times1$ supercell, corresponding to a doubling of the in-plane unit cell. We then use these force constants to compute zone-center phonon frequencies and eigenvectors.

Table S2 compares the DFT zone-center frequencies of infrared-active phonons with the mode frequencies extracted from Drude-Lorentz fits at 160 K and 4 K. At 160 K, above the density-wave transition, we associate the fitted out-of-plane modes with nearby calculated infrared-active modes based on frequency proximity and the calculated oscillator strengths of the out-of-plane dipole component. By contrast, at 4 K (below T_{DW}) we resolve additional phonon modes that have no direct counterparts among the calculated modes.

TABLE S2. Comparison of extracted phonon modes from Drude-Lorentz fits at 160 K and 4 K to calculated infrared-active phonon modes. The DFT mode labels ($P\#$) follow the ranking of the phonon frequencies among all 102 calculated modes. Irreps denote irreducible representations.

DFT modes	**Irreps**	**DFT (cm^{-1})**	**160 K fit (cm^{-1})**	**4 K fit (cm^{-1})**
$P18$	B_u	120.6	119.6 ± 0.1	120.5 ± 0.1
$P20$	B_u	125.5	132.0 ± 0.3	133.9 ± 0.2
$P23$	B_u	137.3	140.9 ± 0.4	142.0 ± 0.3
$P26$	B_u	144.2	153.5 ± 0.3	154.4 ± 0.3
$P28$	B_u	152.1	$168.8 \pm < 0.1$	$169.2 \pm < 0.1$
$P46$	B_u	227.5	225.9 ± 0.8	225.9 ± 0.6
$P48$	B_u	234.0	251.6 ± 0.7	249.2 ± 1.1
$P54$	B_u	268.3	270.0 ± 0.7	266.1 ± 0.6
$P57$	B_u	286.2	285.6 ± 0.4	282.8 ± 0.2
$P60$	B_u	296.0	289.3 ± 0.1	$289.5 \pm < 0.1$
$P62$	B_u	303.8	309.0 ± 0.1	310.2 ± 0.1
$P64$	B_u	307.6	314.0 ± 0.2	315.8 ± 0.1
$P68$	A_u	316.4	323.1 ± 0.6	325.8 ± 0.4
$P76$	B_u	353.3	340.6 ± 0.1	337.1 ± 0.3
				342.8 ± 0.3
$P81$	B_u	390.9	$371.3 \pm < 0.1$	369.9 ± 0.1
				375.6 ± 0.1
$P86$	B_u	434.4	425.0 ± 0.1	431.6 ± 0.1
$P93$	B_u	501.1	471.6 ± 0.2	472.0 ± 0.2
$P100$	B_u	573.9	554.5 ± 1.2	558.9 ± 3.6

S9. PHONON MODES: ANOMALY AND ATOMIC DISPLACEMENT

Across the DW transition, reported lattice-parameter anomalies are well below the level of 0.1% in relative magnitude [1, 18, 19, 21]. A simple way to estimate the size of phonon shifts expected from such small structural changes is via a mode Grüneisen parameter γ_i, defined by

$$\frac{\Delta\omega_i}{\omega_i} \approx -\gamma_i \frac{\Delta V}{V}, \tag{S4}$$

(or an anisotropic analog using linear strains). The Grüneisen parameter, γ_i, is usually of order unity for common solid-state materials, even taking a conservative upper bound $\gamma_i \sim$ 2-3 [23, 24], lattice/volume changes below the 0.1% level would imply $\Delta\omega/\omega \lesssim$ 0.1%-0.3%. This estimate is well below the $\sim$ 1% frequency anomalies and splittings we observe, and, importantly, such anomalies are highly mode-selective (confined to the 300-500 cm^{-1} window) rather than a broadly distributed hardening/softening expected from uniform strain. This comparison supports that the dominant phonon renormalization is tied to the DW electron-phonon/magnetoelastic coupling rather than a simple structural anomaly.

To quantify the temperature dependence of the phonon anomalies, we analyze the evolution of phonon frequency $\omega_0(T)$ and scattering rate (linewidth) $\gamma(T)$ extracted from the Drude-Lorentz fits. The high-temperature behavior is described by the Klemens-Hart-Aggarwal-Lax model [25]. In this model, cubic anharmonic decay of phonons gives the temperature dependence of the phonon frequency and the scattering rate as

$$\begin{aligned} \omega_0(T) &= \omega_{0,T=0} + A \cdot \left(1 + \frac{2}{e^x - 1}\right), \\ \gamma(T) &= \gamma_{\text{res}} + B \cdot \left(1 + \frac{2}{e^x - 1}\right), \end{aligned} \tag{S5}$$

with $x = \frac{\hbar\omega_{0,T=0}}{2k_B T}$.

Here, $\omega_{0,T=0}$ denotes the bare phonon frequency at zero temperature, γ_{res} represents a temperature-independent residual scattering rate that captures additional broadening mechanisms not accounted for by anharmonic decay, and A, B are constants. Fits using these expressions are restricted to the high-temperature regime, and deviations from the extrapolated behavior at low temperatures reflect strong phonon renormalization induced by the DW transition.

The phonon anomalies induced by the DW transition are found primarily in the frequency range between 300 and 500 cm^{-1}. We therefore focus on four phonon modes in this window that exhibit the most pronounced deviations from conventional anharmonic behavior. Two phonon peaks, located near 371 cm^{-1} (Fig. S15) and 340 cm^{-1} (Fig. S16) in the high-temperature phase, split into distinct branches upon cooling to the DW state. In addition, two higher-frequency modes near 430 cm^{-1} (Fig. S17) and 475 cm^{-1} (Fig. S18) show strong renormalization without a resolvable splitting. For all four modes, the temperature dependence of the resonance frequency and linewidth is analyzed using the anharmonic decay model described above. By contrast, phonon modes outside this frequency window, such as the mode near 169 cm^{-1} shown in Fig. S21, exhibit temperature evolutions that remain well described by conventional anharmonic behavior over the full temperature range. This comparison highlights the non-uniform and energy-selective nature of the DW-phonon coupling, with the strongest deviations from anharmonicity occurring for modes in the frequency range between approximately 370 and 430 cm^{-1}. Notably, this range coincides with the typical energy scale of Ni-O bond-stretching vibrations, suggesting that lattice distortions involving Ni-O bonds are particularly sensitive to the electronic modulation associated with the DW transition. To further elucidate the lattice degrees of freedom underlying the phonon anomalies, we examine the calculated displacement patterns of the four representative modes discussed above. As shown in Fig. S19, these modes are dominated by Ni-O bond bending, suggesting that Ni-O distortions are especially sensitive to the electronic reconstruction across the DW transition. Consistent with this interpretation, additional DFT calculated eigenvectors for other modes in the same 300-500 cm^{-1} window also exhibit substantial participation of the Ni-O bonds, even though these modes are not associated with experimentally observed phonons (Fig. S20).

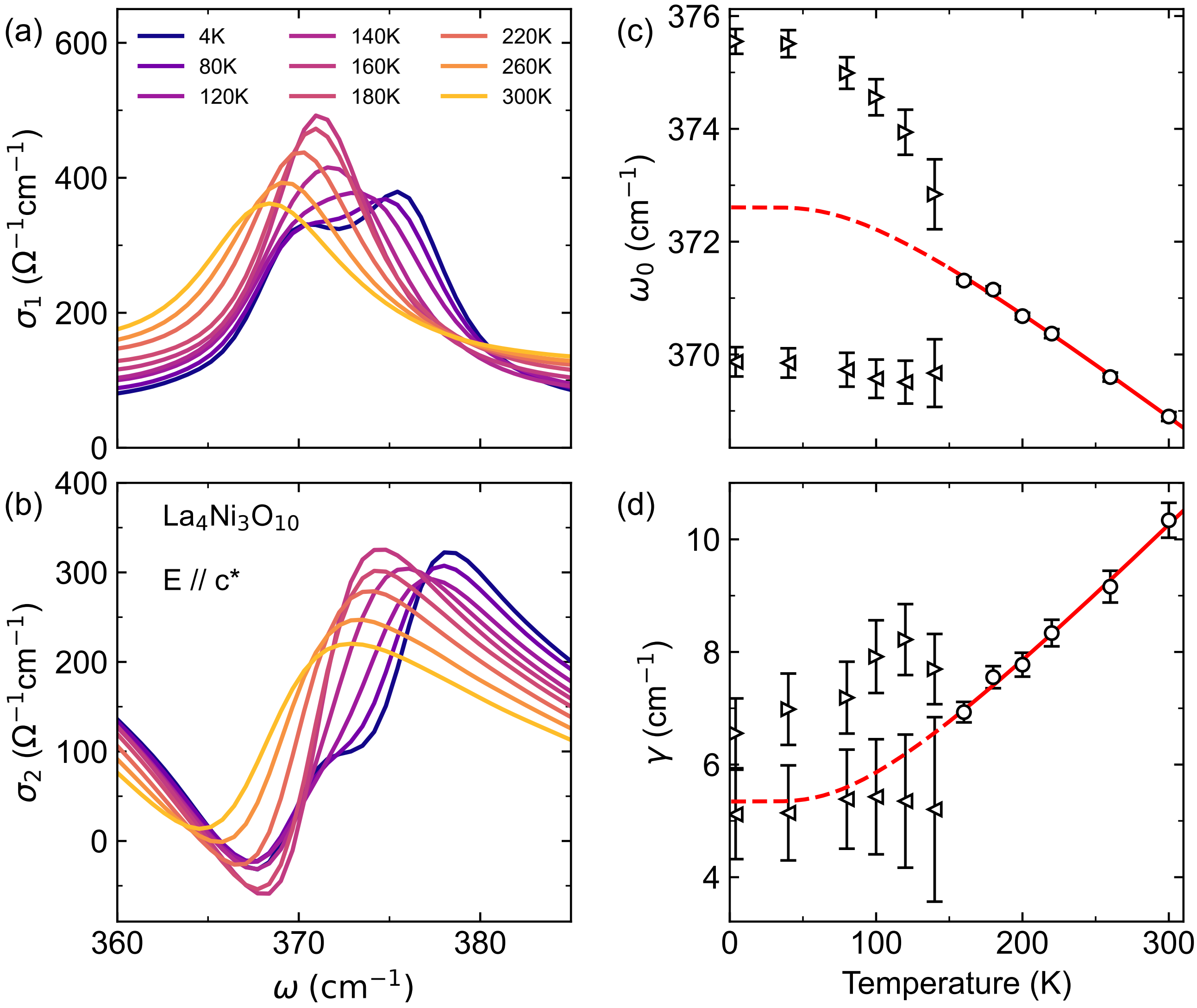

FIG. S15. (a), (b) Real and imaginary out-of-plane optical conductivity of $La_4Ni_3O_{10}$ in a narrow frequency window around the 371 cm^{-1} mode. (c), (d) Temperature dependence of the fitted phonon frequency ω_0 and scattering rate γ for the modes near 371 cm^{-1}. On cooling below the density-wave (DW) transition, this phonon peak splits into two distinct low-temperature branches that evolve from a single high-temperature mode. Solid red curves show anharmonic phonon-decay fits to the high-temperature data, and dashed curves extrapolate the fits to low temperature. The strong deviation of the measured low-temperature phonon parameters from the extrapolated anharmonic trend indicates substantial DW-associated phonon renormalization.

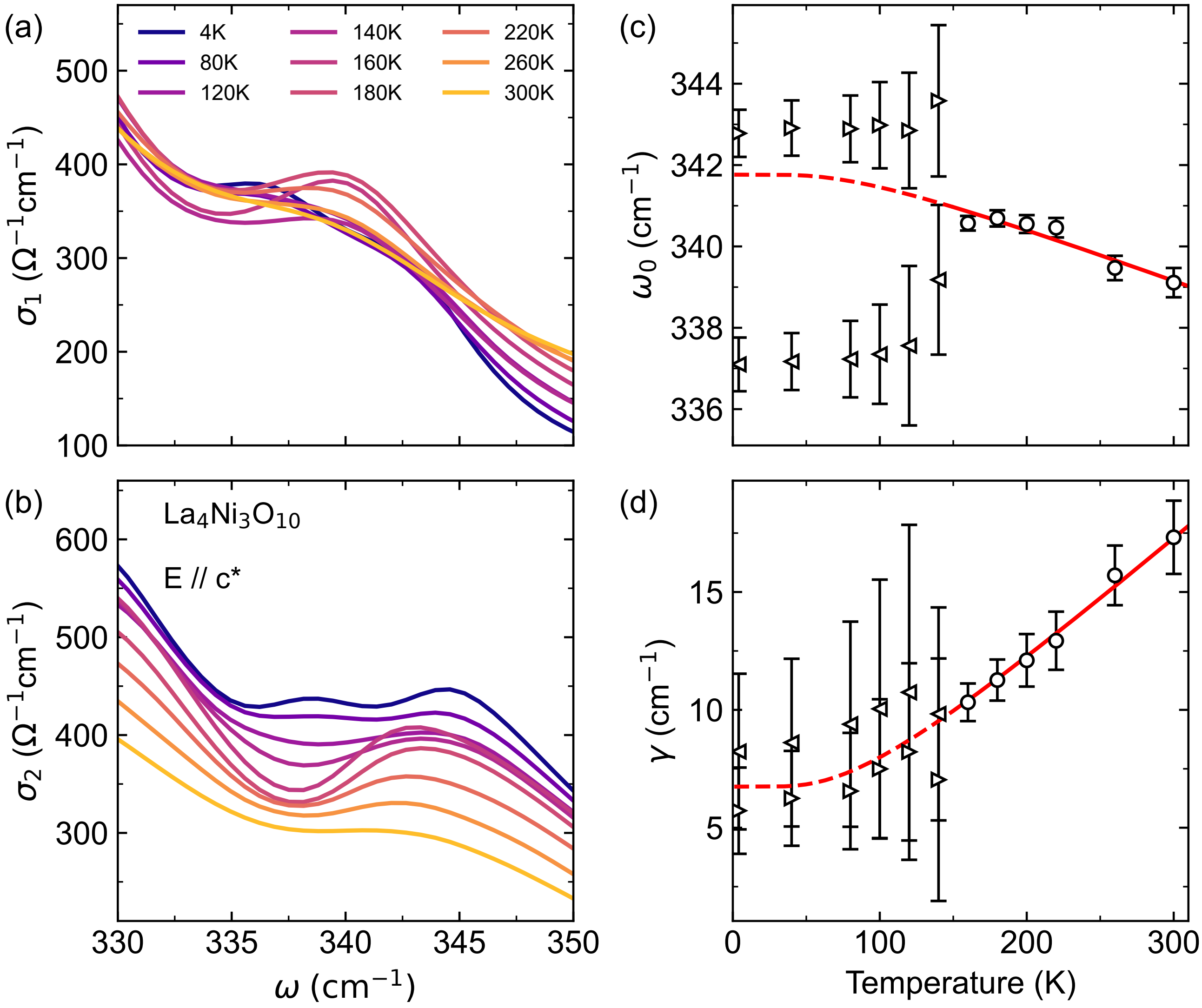

FIG. S16. (a), (b) Real and imaginary out-of-plane optical conductivity of La$_4$Ni$_3$O$_{10}$ in a narrow frequency window around the 340 cm^{-1} mode. (c), (d) Temperature dependence of the fitted phonon frequency ω_0 and scattering rate γ for the modes near 340 cm^{-1}. The phonon exhibits a subtle splitting below the DW transition, most clearly resolved in the imaginary part of the optical conductivity $\sigma_2(\omega)$. Solid red curves represent fits to the high-temperature data using an anharmonic phonon decay model, whereas dashed lines indicate extrapolations into the low-temperature regime. The deviation between the low-temperature phonon parameters and the extrapolated anharmonic behavior reflects a DW-induced phonon renormalization.

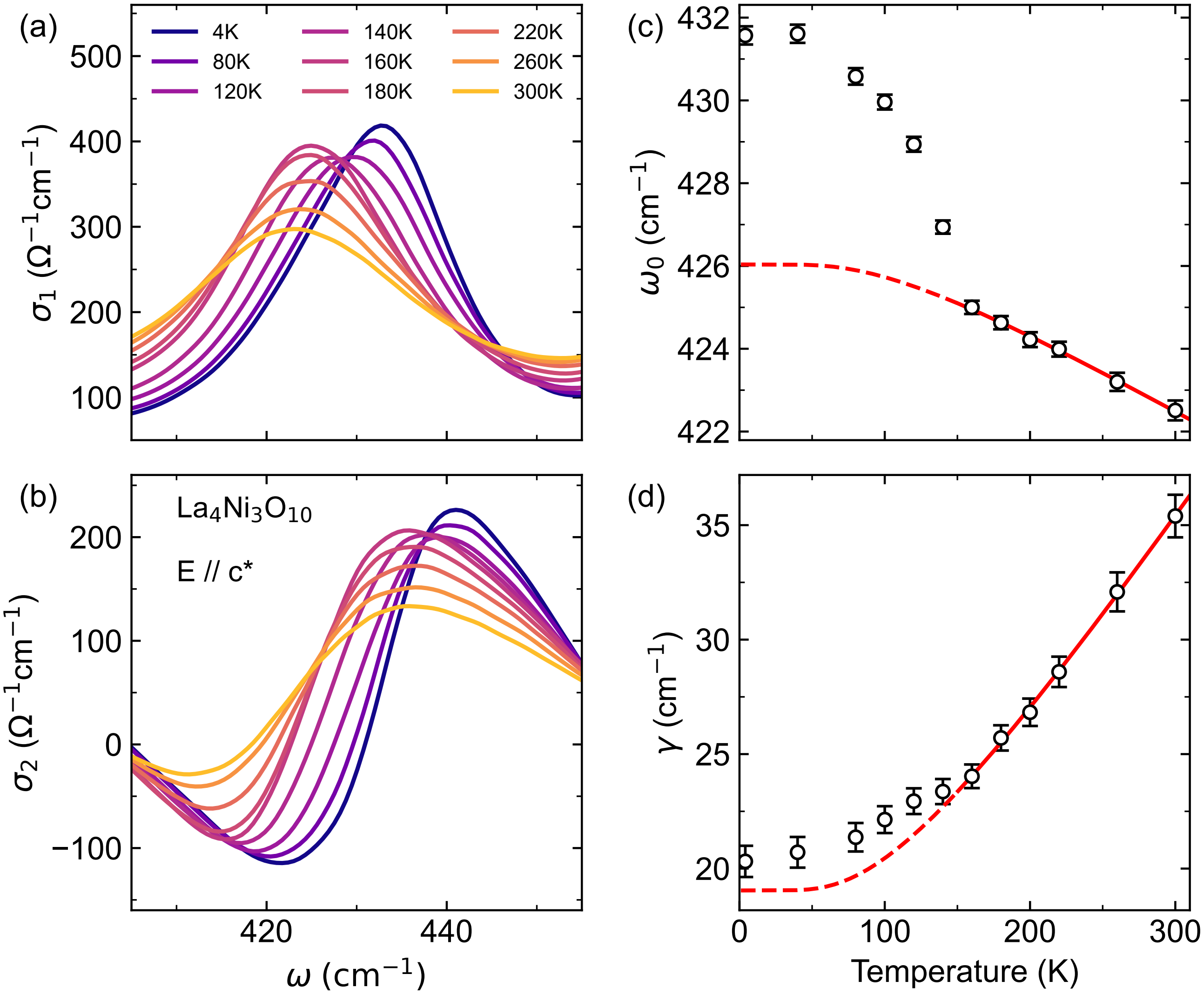

FIG. S17. (a), (b) Real and imaginary out-of-plane optical conductivity of La$_4$Ni$_3$O$_{10}$ in a narrow frequency window around the 430 cm^{-1} mode. (c), (d) Temperature dependence of the fitted phonon frequency ω_0 and scattering rate γ for the modes near 430 cm^{-1}. Unlike the lower-energy modes, this phonon shows no resolvable splitting, but its frequency and linewidth renormalize strongly on cooling below the DW transition. Solid red curves show anharmonic phonon-decay fits to the high-temperature data, and dashed curves extrapolate the fits to low temperature. The marked deviation of the low-temperature phonon parameters from the extrapolated anharmonic trend signals strong DW-induced renormalization.

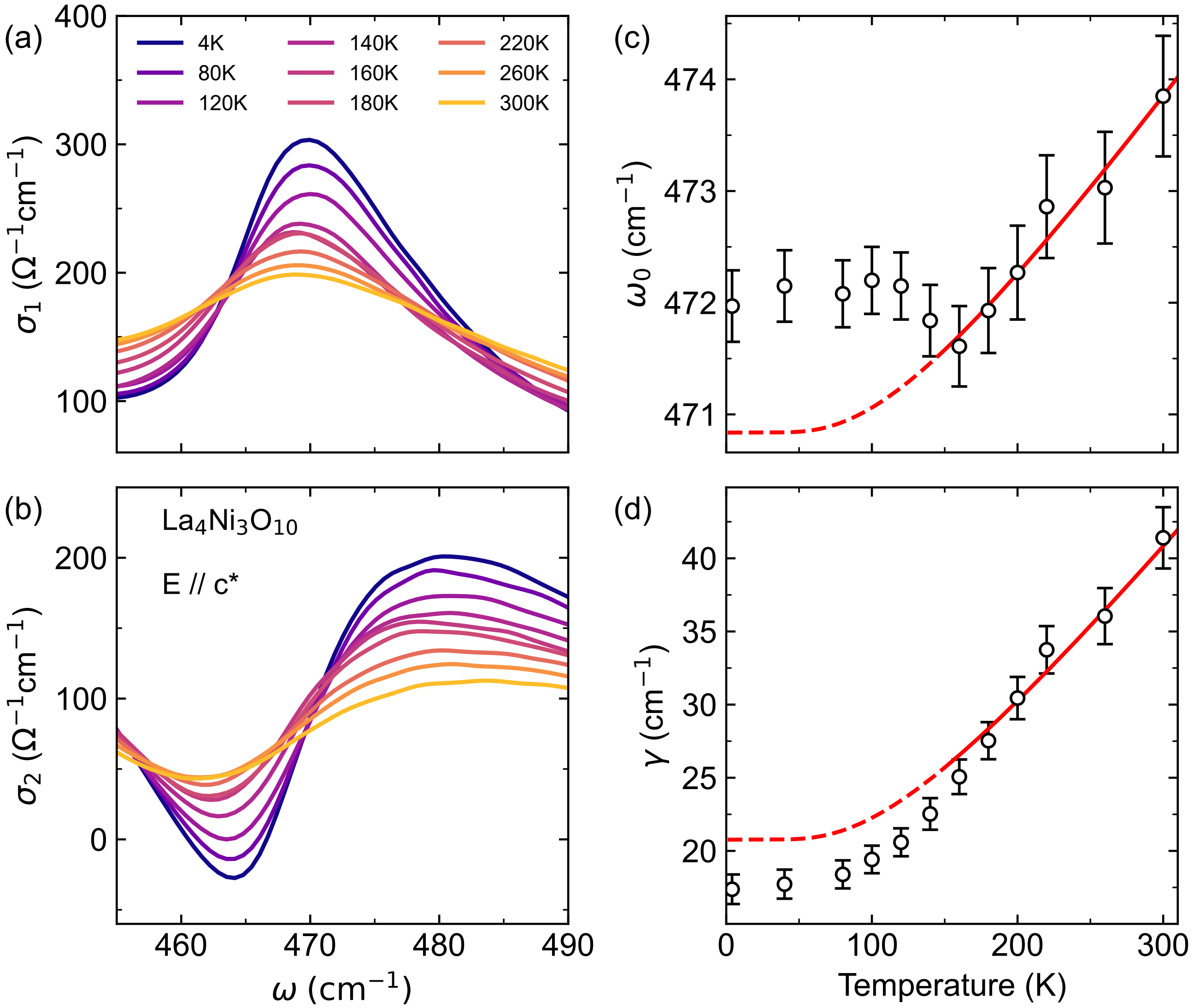

FIG. S18. (a), (b) Real and imaginary out-of-plane optical conductivity of La$_4$Ni$_3$O$_{10}$ in a narrow frequency window around the 475 cm^{-1} mode. (c), (d) Temperature dependence of the fitted phonon frequency ω_0 and scattering rate γ for the modes near 475 cm^{-1}. As for the mode near 430 cm^{-1}, this phonon shows no clear splitting but undergoes a strong renormalization of its frequency and linewidth below the DW transition. Solid red curves show anharmonic phonon-decay fits to the high-temperature data, and dashed curves extrapolate the fits to low temperature. The deviation of the measured low-temperature parameters from the extrapolated anharmonic trend further highlights the strong impact of the DW transition on the lattice dynamics.

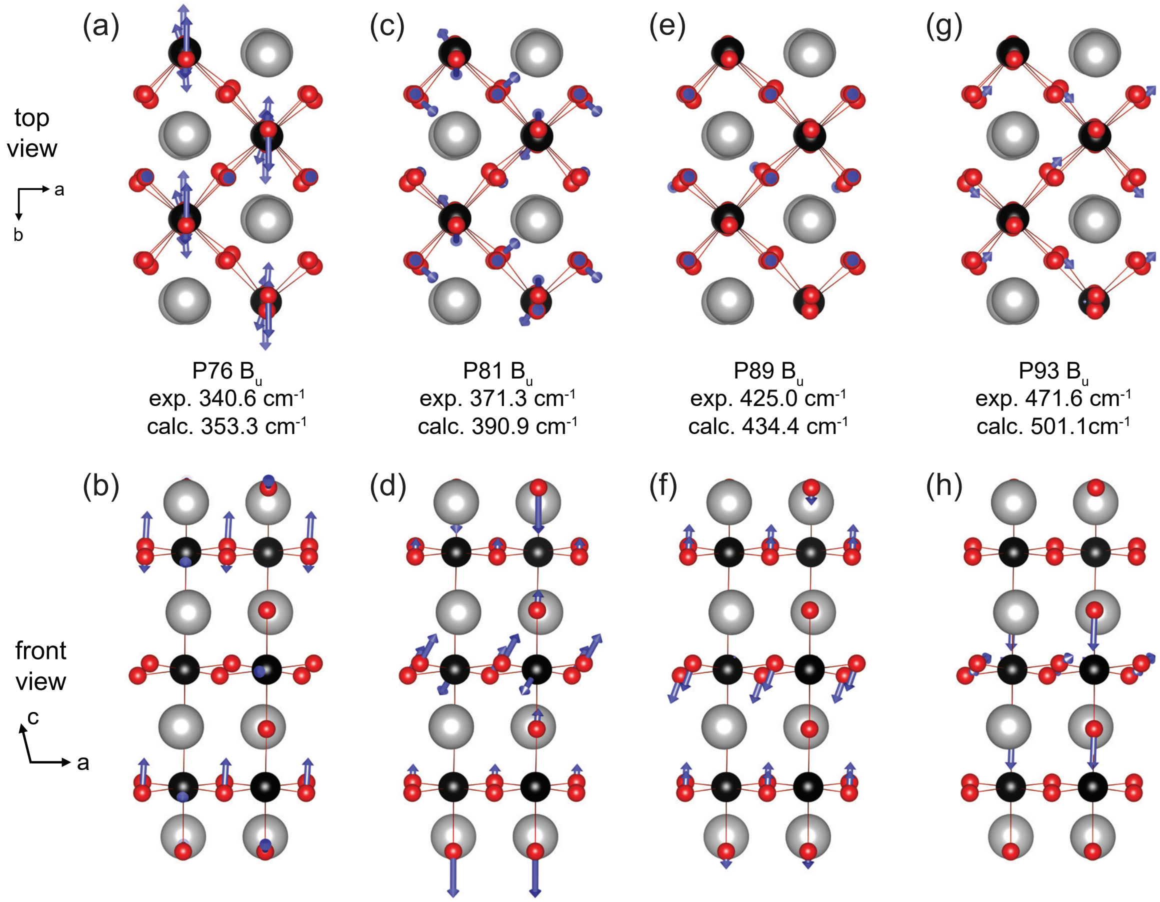

FIG. S19. Calculated atomic displacement patterns for four representative infrared-active phonon modes that exhibit pronounced anomalies across the density-wave transition. Panels (a,b), (c,d), (e,f), and (g,h) show the top and front views of the phonon eigenvectors for modes near 340 cm^{-1} (P76), 371 cm^{-1} (P81), 430 cm^{-1} (P86), and 475 cm^{-1} (P93), respectively. The corresponding experimental (at 160 K) and calculated phonon frequencies are indicated for each mode. The mode labels (P#) follow the ranking of the phonon frequencies among all 102 calculated zone-center phonon modes, consistent with the notation used in Table S2. For clarity, only displacements with large amplitude are shown for each mode.

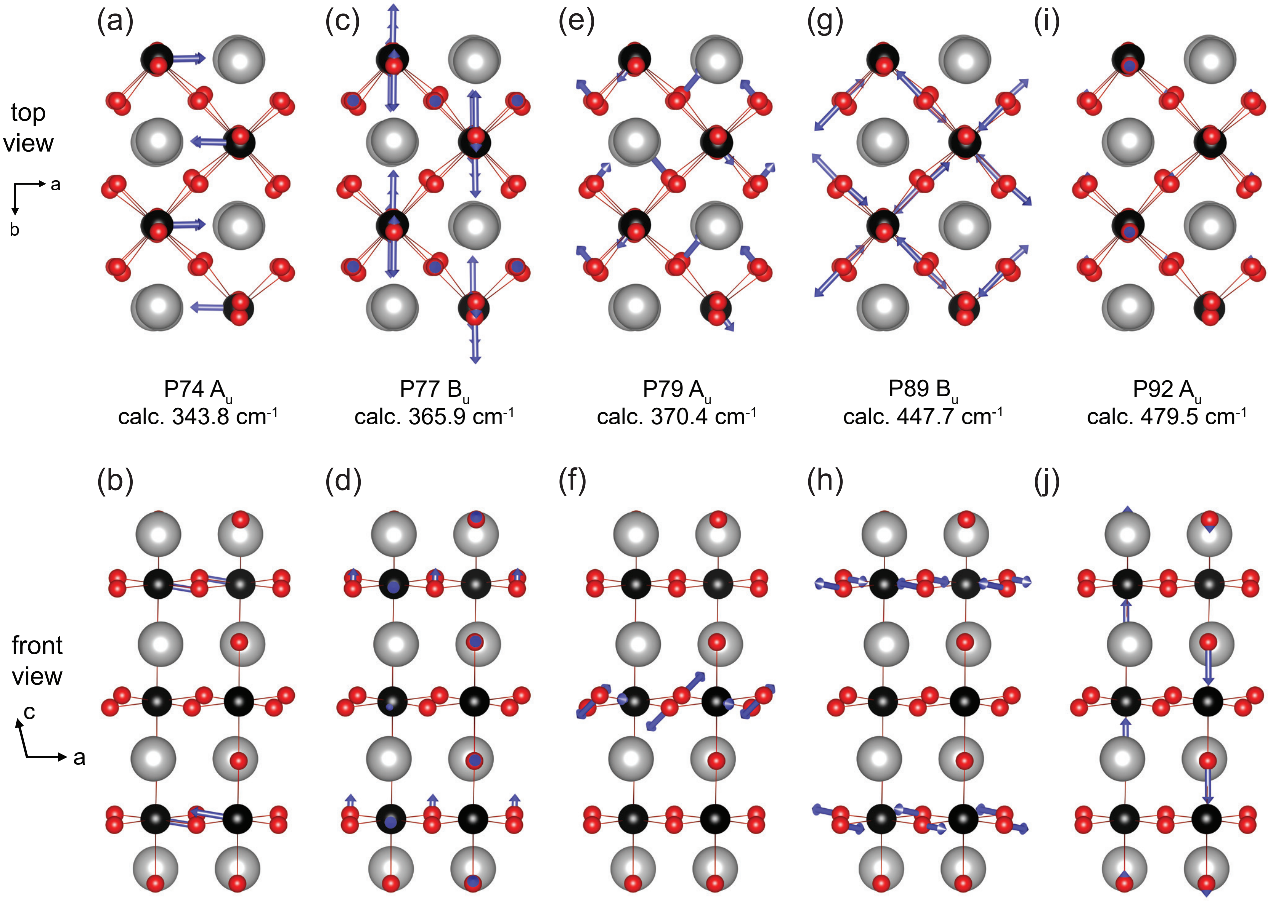

FIG. S20. Calculated atomic displacement patterns for other infrared-active phonon modes in the frequency range between 300 and 500 cm^{-1}. Panels (a,b), (c,d), (e,f), (g,h), and (i,j) show the top and front views of the phonon eigenvectors for modes P74, P77, P79, P89, and P92, respectively. The corresponding calculated phonon frequencies are indicated for each mode. The mode labels (P#) follow the ranking of the phonon frequencies among all 102 calculated zone-center phonon modes. For clarity, only displacements with large amplitude are shown for each mode. These representative eigenvectors illustrate that phonons in this frequency window primarily involve vibrations of the Ni-O bonds (including Ni-O stretching and bending character), consistent with the discussion in the main text.

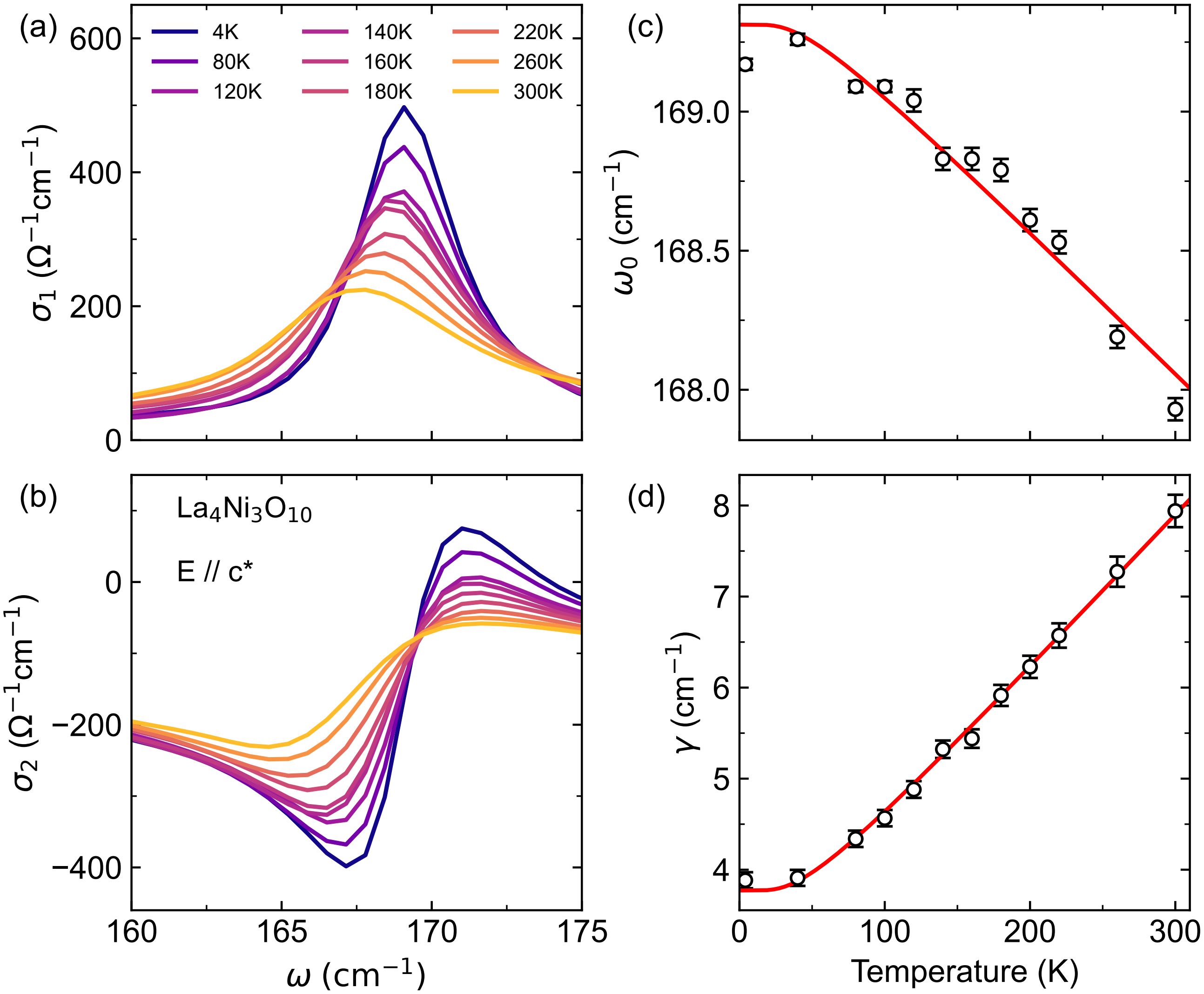

FIG. S21. (a), (b) Real and imaginary out-of-plane optical conductivity of $La_4Ni_3O_{10}$, in a narrow frequency window around the 169 cm^{-1} mode. (c), (d) Temperature dependence of the fitted phonon frequency ω_0 and scattering rate γ for the modes. In contrast to the pronounced anomalies of selected modes between 300 and 500 cm^{-1}, the phonon near 169 cm^{-1} shows no discernible renormalization of its frequency or linewidth across the DW transition. Solid red curves show anharmonic phonon-decay fits over the full temperature range. The good agreement indicates that this mode is largely insensitive to the DW transition, underscoring the mode and energy selectivity of DW-induced phonon modulation.

S10. HOPPING PARAMETERS: NONMAGNETIC AND SPIN DENSITY WAVE STATES

To further quantify the electronic reconstruction, we calculate representative hopping parameters for $La_4Ni_3O_{10}$ in the nonmagnetic state and in our approximation to the intertwined CDW+SDW state in a $\sqrt{2}\times\sqrt{2}$ cell, that we call M/0/M. This magnetic state consists of outer layers that are antiferromagnetically coupled (both in and out-of-plane) and a nonmagnetic inner layer, as described in Ref. [26]. The M/0/M state qualitatively agrees with the intensity distribution of the superlattice reflections derived from single-crystal neutron diffraction [27]. We choose this state given the complications associated with simulations that could account for the incommensurate q_{DW} of $La_4Ni_3O_{10}$, whose closest commensurate analog is a 5-period stripe in the plane. The hopping amplitudes for these two magnetic states are obtained by constructing maximally localized Wannier functions (MLWFs) for the two Ni-e_g orbitals (d_{z^2} and $d_{x^2-y^2}$) using the Wannier90 package [28]. GGA+U calculations [29] are performed with $U_{\text{eff}} = 4.0$ eV. A fine k-mesh of $9 \times 9 \times 2$ is used.

The largest hopping terms (listed in Table S3) are $t_\perp^z$, which represents the interlayer d_{z^2} hopping; $t_\parallel^x$, which denotes the in-plane $d_{x^2-y^2}$ hopping; and $t_\parallel^{xz}$, which describes the in-plane hybridization between $d_{x^2-y^2}$ and d_{z^2}. The $t_\perp^z$ hopping reflects the strong vertical overlap of the d_{z^2}-derived states across adjacent Ni-O layers, $t_\parallel^x$ and $t_\parallel^{xz}$ characterize the in-plane charge dynamics dominated by $d_{x^2-y^2}$ orbitals. A comparison of hopping amplitudes between the two states shows that the SDW order substantially reduces the magnitude of $t_\perp^z$, from -0.539 to -0.375 eV, indicating a pronounced weakening of the interlayer d_{z^2}-mediated coupling within the trilayer. Because this hopping channel governs the out-of-plane charge dynamics, its suppression provides a natural microscopic counterpart to the optical result that c^*-axis transport is strongly suppressed in the DW phase. In this sense, the hopping analysis is consistent with the mechanism discussed in the main text: the density-wave state reconstruction weakens the effective interlayer overlap and thereby promotes electronic layer decoupling. The remaining hopping parameters change less dramatically and do not alter this central conclusion.

TABLE S3. Effective hopping parameters (in eV) for trilayer $La_4Ni_3O_{10}$ at ambient pressure in the nonmagnetic and spin-density-wave (SDW, M/0/M) states. Here, $t_\perp^z$ denotes the interlayer d_{z^2}-d_{z^2} hopping within a trilayer block, $t_\parallel^x$ the nearest-neighbor in-plane $d_{x^2-y^2}$-$d_{x^2-y^2}$ hopping, and $t_\parallel^{xz}$ the nearest-neighbor in-plane interorbital $d_{x^2-y^2}$-d_{z^2} hybridization. TLi and TLo denote the inner and outer Ni-O layers of the trilayer block, respectively.

	Ni	Nonmagnetic	M/0/M
$t_\perp^z$		-0.539	-0.375
$t_\parallel^x$	TLi	-0.404	-0.414
	TLo	-0.408	-0.460
$t_\parallel^{xz}$	TLi	-0.238	-0.250
	TLo	-0.207	-0.156

---

[1] J. Zhang, H. Zheng, Y.-S. Chen, Y. Ren, M. Yonemura, A. Huq, and J. F. Mitchell, High oxygen pressure floating zone growth and crystal structure of the metallic nickelates $R_4Ni_3O_{10}$ ($R = \mathrm{La, Pr}$), Phys. Rev. Mater. **4**, 083402 (2020).

[2] C. C. Homes, M. Reedyk, D. A. Cradles, and T. Timusk, Technique for measuring the reflectance of irregular, submillimeter-sized samples, Appl. Opt. **32**, 2976 (1993).

[3] C. C. Homes, J. M. Tranquada, and D. J. Buttrey, Stripe order and vibrational properties of $La_2NiO_{4+\delta}$ for $\delta = 2/15$: measurements and *ab initio* calculations, Phys. Rev. B **75**, 045128 (2007).

[4] H. Padma, F. Glerean, S. F. R. TenHuisen, Z. Shen, H. Wang, L. Xu, J. D. Elliott, C. C. Homes, E. Skoropata, H. Ueda, B. Liu, E. Paris, A. Romaguera, B. Lee, W. He, Y. Wang, S. H. Lee, H. Choi, S.-Y. Park, Z. Mao, M. Calandra, H. Jang, E. Razzoli, M. P. M. Dean, Y. Wang, and M. Mitrano, Symmetry-protected electronic metastability in an optically driven cuprate ladder, Nat. Mater. **24**, 1584 (2025).

[5] F. Y. Gao, Z. Zhang, Z.-J. Liu, and K. A. Nelson, High-speed two-dimensional terahertz spectroscopy with echelon-based shot-to-shot balanced detection, Opt. Lett. **47**, 3479 (2022).

[6] D. B. Tanner, Use of x-ray scattering functions in Kramers-Kronig analysis of reflectance, Phys. Rev. B **91**, 035123 (2015).

[7] P. Blaha, K. Schwarz, F. Tran, R. Laskowski, G. K. H. Madsen, and L. D. Marks, WIEN2k: An APW+lo program for calculating the properties of solids, J. Chem. Phys. **152**, 074101 (2020).

[8] J. P. Perdew, K. Burke, and M. Ernzerhof, Generalized gradient approximation made simple, Phys. Rev. Lett. **77**, 3865 (1996).

[9] A. Seidl, A. Görling, P. Vogl, J. A. Majewski, and M. Levy, Generalized Kohn-Sham schemes and the band-gap problem, Phys. Rev. B **53**, 3764 (1996).

[10] H. Li, X. Zhou, T. Nummy, J. Zhang, V. Pardo, W. E. Pickett, J. F. Mitchell, and D. S. Dessau, Fermiology and electron dynamics of trilayer nickelate $La_4Ni_3O_{10}$, Nat. Commun. **8**, 704 (2017).

[11] S. Xu, C.-Q. Chen, M. Huo, D. Hu, H. Wang, Q. Wu, R. Li, D. Wu, M. Wang, D.-X. Yao, T. Dong, and N. Wang, Origin of the density wave instability in trilayer nickelate $La_4Ni_3O_{10}$ revealed by optical and ultrafast spectroscopy, Phys. Rev. B **111**, 075140 (2025).

[12] M. R. Norman, Landau theory of the density wave transition in trilayer Ruddlesden-Popper nickelates, Phys. Rev. B **112**, 075149 (2025).

[13] M. M. Qazilbash, J. J. Hamlin, R. E. Baumbach, L. Zhang, D. J. Singh, M. B. Maple, and D. N. Basov, Electronic correlations in the iron pnictides, Nat. Phys. **5**, 647 (2009).

[14] L. Degiorgi, Electronic correlations in iron-pnictide superconductors and beyond: lessons learned from optics, New J. Phys. **13**, 023011 (2011).

[15] Z. Liu, J. Li, M. Huo, B. Ji, J. Hao, Y. Dai, M. Ou, Q. Li, H. Sun, B. Xu, Y. Lu, M. Wang, and H.-H. Wen, Evolution of electronic correlations in the Ruddlesden-Popper nickelates, Phys. Rev. B **111**, L220505 (2025).

[16] Z. Liu, M. Huo, J. Li, Q. Li, Y. Liu, Y. Dai, X. Zhou, J. Hao, Y. Lu, M. Wang, and H.-H. Wen, Electronic correlations and partial gap in the bilayer nickelate $La_3Ni_2O_7$, Nat. Commun. **15**, 7570 (2024).

[17] M. Dressel and G. Grüner, *Electrodynamics of solids: optical properties of electrons in matter* (Cambridge University Press, 2002).

[18] D. Rout, S. R. Mudi, M. Hoffmann, S. Spachmann, R. Klingeler, and S. Singh, Structural and physical properties of trilayer nickelates $R_4Ni_3O_{10}$ ($R = \mathrm{La, Pr, Nd}$), Phys. Rev. B **102**, 195144 (2020).

[19] S. Kumar, Ø. Fjellvåg, A. O. Sjåstad, and H. Fjellvåg, Physical properties of Ruddlesden-Popper ($n = 3$) nickelate: $La_4Ni_3O_{10}$, Journal of Magnetism and Magnetic Materials **496**, 165915 (2020).

[20] S. Huangfu, G. D. Jakub, X. Zhang, O. Blacque, P. Puphal, E. Pomjakushina, F. O. von Rohr, and A. Schilling, Anisotropic character of the metal-to-metal transition in $Pr_4Ni_3O_{10}$, Phys. Rev. B **101**, 104104 (2020).

[21] N. Li, J. Guan, L. Yan, X. Yan, M. Li, X. Liu, K. Zhang, F. Li, S. Cai, H. Dong, A. N-Diaye, M. Amboage, J. Zhang, Y. Cao, H. Guo, Q. Kong, L. Sun, and W. Yang, Crystal and electronic structure studies of $La_4Ni_3O_{10-\delta}$ under high-pressure and low-temperature conditions, J. Am. Chem. Soc. **147**, 43717 (2025).

[22] A. Togo and I. Tanaka, First principles phonon calculations in materials science, Scripta Materialia **108**, 1 (2015).

[23] R. Boehler and J. Ramakrishnan, Experimental results on the pressure dependence of the grüneisen parameter: a review, J. Geophys. Res. **85**, 6996 (1980).

[24] R. J. Bruls, H. T. Hintzen, G. de With, R. Metselaar, and J. C. van Miltenburg, The temperature dependence of the grüneisen parameters of $MgSiN_2$, AlN and β-Si_3N_4, J. Phys. Chem. Solids **62**, 783 (2001).

[25] M. Balkanski, R. F. Wallis, and E. Haro, Anharmonic effects in light scattering due to optical phonons in silicon, Phys.

Rev. B **28**, 1928 (1983).

[26] H. LaBollita, J. Kapeghian, M. R. Norman, and A. S. Botana, Electronic structure and magnetic tendencies of trilayer $La_4Ni_3O_{10}$ under pressure: Structural transition, molecular orbitals, and layer differentiation, Phys. Rev. B **109**, 195151 (2024).

[27] J. Zhang, D. Phelan, A. S. Botana, Y.-S. Chen, H. Zheng, M. Krogstad, S. G. Wang, Y. Qiu, J. A. Rodriguez-Rivera, R. Osborn, S. Rosenkranz, M. R. Norman, and J. F. Mitchell, Intertwined density waves in a metallic nickelate, Nat. Commun. **11**, 6003 (2020).

[28] G. Pizzi, V. Vitale, R. Arita, S. Blügel, F. Freimuth, G. Géranton, M. Gibertini, D. Gresch, C. Johnson, T. Koretsune, *et al.*, Wannier90 as a community code: new features and applications, J. Phys.: Condens. Matter. **32**, 165902 (2020).

[29] S. L. Dudarev, G. A. Botton, S. Y. Savrasov, C. J. Humphreys, and A. P. Sutton, Electron-energy-loss spectra and the structural stability of nickel oxide: An LSDA+U study, Phys. Rev. B **57**, 1505 (1998).